

FULL PAPER

Open Access



# A low-dispersion spectral video camera for observing lunar impact flashes

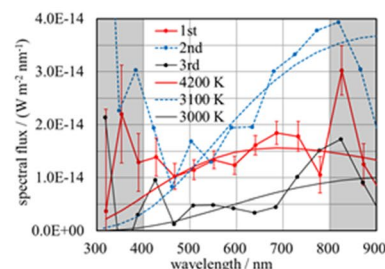
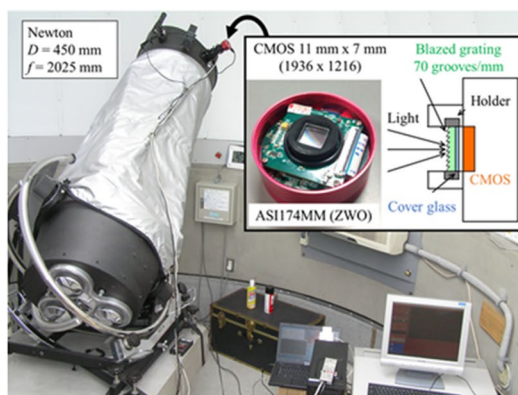
Masahisa Yanagisawa<sup>1,2\*</sup> and Fumihiro Kakinuma<sup>1</sup>

## Abstract

An impact of a meteoroid on the lunar surface at speeds exceeding several kilometers per second generates a light flash generally less than 0.1 s in duration. We made a simple spectral video camera for observing the lunar impact flashes and monitored the waxing crescent Moon's non-sunlit surface from Oct. 2016 to May 2017. We detected ten flash candidates though there was no report of simultaneous detections by other observers. We obtained low-dispersion spectra in visible wavelengths for nine of them. Six of them show spectra similar to those of the flashes observed during the Geminids meteor activity in Dec. 2018 by the same camera. The spectra are continuous and red. Blackbody spectra fitted to them show temperatures around 3000 K. On the other hand, three of them show continuous blue spectra. Blackbody spectra fitted to them show temperatures of more than 6000 K. Specular reflection of sunlight by space debris might lead to these flashes. However, the impact of a low-density meteoroid not against the fine lunar regolith but solid lunar rocks could cause blue flashes. In this paper, we give full details of the camera and the analytical procedures of the videos. We also discuss recommendations for future spectral observations.

**Keywords:** Spectral video camera, Spectrum, Lunar impact flash

## Graphical Abstract



The temporal evolution of the spectrum of a lunar impact flash on Feb. 1, 2017, observed by our simple spectral camera (figure to the left). The frame interval is 20 milli-sec. Smooth curves show blackbody spectra best-fitted to the plots.

\*Correspondence: yanagi.uec@gmail.com

<sup>2</sup> Present Address: Tama-shi, Tokyo 206-0034, Japan

Full list of author information is available at the end of the article

## Introduction

At collisions in the solar system, there are many cases where the meteoroids' impacts against solid planetary surfaces occur at speeds exceeding  $10 \text{ km s}^{-1}$ , which almost cannot be reproduced in laboratory experiments (e.g., Kurosawa et al. 2012). In such a collision, melting, evaporation, and ionization of silicates, which are not the dominant processes in the lower-speed impacts, occur. Therefore, understanding the high-speed collisions accompanying such processes is an essential issue in planetary sciences. Experimental and theoretical efforts to describe the processes have been made (e.g., Schultz and Eberhardy 2015; Nemtchinov et al. 1998a, b). However, the processes have not been studied well by observing natural high-speed collisions. Lunar impact flashes by meteoroids at several tens of kilometers per second provide an opportunity for observational studies of the high-speed collisions (Yanagisawa et al. 2021, hereafter Paper I).

Spectral information is essential to study the high-speed impact phenomena in laboratory experiments (e.g., Schultz and Eberhardy 2015). However, spectral observations of the lunar impact flashes are not easy. The flashes are rare temporal events, and their duration is usually less than 0.1 s. We cannot predict where a flash occurs on the lunar disk nor how bright it is. Therefore, the large field of view (e.g.,  $0.5^\circ$ , the angular diameter of the lunar disk) is desirable to increase the number of detections.

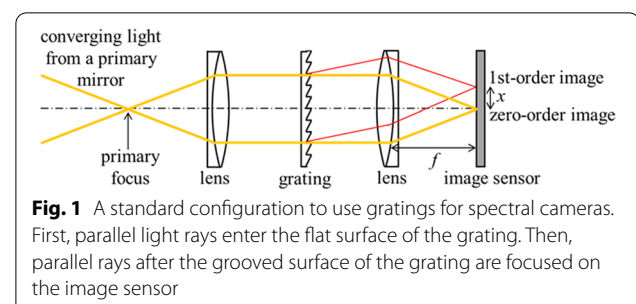
We monitor the Moon's night-side by video cameras, but the lunar surface illuminated by the Earth is not so dark as the night sky (Montanes-Rodriguez et al. 2007). Therefore, the exposure time of the cameras must be short enough to reduce the background level. At the same time, the non-exposure duration between video frames must be minimized not to miss the flashes that occur in the duration. The short exposure time with the minimum inter-frame duration requires a high framing rate of the cameras. Large image sensors with many pixels for the large field of view, used in many astronomical observatories, need some time to transfer image data to computers. Therefore, they are not appropriate for the high framing rate, for example, more than 30 frames per second.

A grating disperses the incoming light into a telescope in spectral observations. It spreads the light over an elongated area on an image sensor. As a result, much more light is necessary than non-spectral observations (a lunar impact flash appears as a point source image) to increase the spectral image's signal-to-noise ratio. Thus, large aperture telescopes are desired. Unfortunately, the large aperture, the large field of view, and the high framing rate are not very compatible.

Non-spectral observations for the flashes have been conducted since the first confirmations of the 1999 Leonids lunar impact flashes (Dunham et al. 2000; Ortiz et al. 2000; Yanagisawa and Kisaichi 2002). As a continuation of the lunar impact flash survey in Spain (Ortiz et al. 1999), the MIDAS project has observed the flashes since 2011 (reviewed in Madio et al. 2019b). Our group in Japan also conducted observations of the flashes associated with the 1999 Leonids (Yanagisawa and Kisaichi 2002), 2004 Perseids (Yanagisawa et al. 2006), and 2007 Geminids (Yanagisawa et al. 2008). NASA Meteoroid Environment Office conducted a routine monitoring program mainly at Marshall Space Flight Center with telescopes of 350 mm in aperture in 2006–2011 and recorded over 300 flashes for a net observation time of 266.88 h (e.g., Suggs et al. 2014). The NELIOTA project funded by ESA started two-color routine observations in 2017 (Bonanos et al. 2018; Xilouris et al. 2018; Liakos et al. 2020). A telescope in Greece of 1.2 m in aperture and 3.4 m in focal length is dedicated to the project.

However, there has been no report of their spectral observations, except Paper I. They used two simple spectral cameras for visible and near-infrared wavelengths and observed 13 lunar impact flashes associated with the December Geminids activities in 2018. Because of the low spectral resolutions and the cameras' simplicity, the analytical procedures of spectral images are complicated and not fully described in Paper I. We describe the details of one of the cameras used in Paper I and the analytical procedures in this article. We also report the results of 10 lunar impact flash candidates observed when we first started using this camera.

We describe the camera in section "A simple spectral camera", laboratory calibrations in "Laboratory calibration of the spectral camera", our observational results in section "Observations and interpretations", and explain how to derive spectra in section "Spectral analyses". Then, we show the spectra and brightness magnitudes of the lunar impact flash candidates in section "Results". Finally, we discuss recommendations for future spectral observations in section "Discussion".



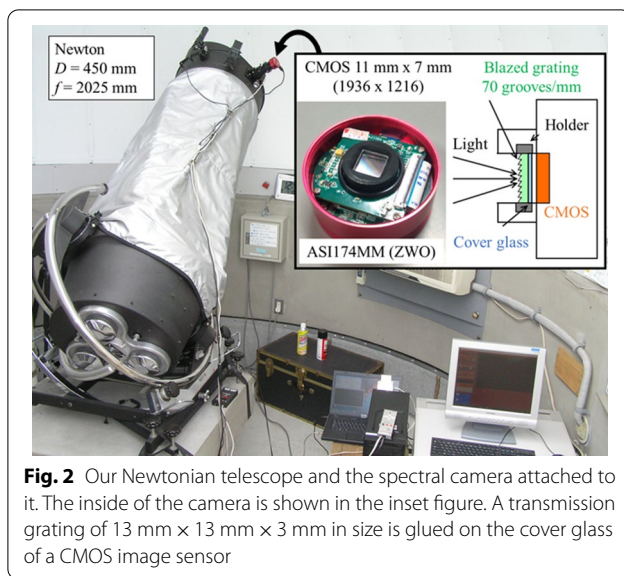


**Fig. 2** Our Newtonian telescope and the spectral camera attached to it. The inside of the camera is shown in the inset figure. A transmission grating of 13 mm × 13 mm × 3 mm in size is glued on the cover glass of a CMOS image sensor

### A simple spectral camera

A lunar impact flash is approximated as a point source in ground-based observations. Its spectral image for a wavelength range appears as a line segment on an image sensor. The extent of the line segment must be long enough to obtain high spectral resolutions. Then, the amount of light that enters into a pixel decreases in the case of continuous spectra. That is, high resolutions lead to dark spectral images. Therefore, we decided to sacrifice the spectral resolution of our camera to make spectral images as bright as possible. We also decided to use a diffraction grating instead of a refraction prism because it is impossible to determine a wavelength in continuous spectral images obtained by a prism.

We do not apply a collimator (or a lens) that makes the converging light from the primary mirror of our telescope into parallel light rays before the grating (Fig. 1). If we use the collimator, the light after the grating must be converged on an image plane by the other lens. The focal length of the lens  $f$ , the spacing of the grating  $\Delta$ , and a wavelength  $\lambda$  determine the distance between the zero-order image and the 1st-order image  $x$ , as  $x \approx f\lambda/\Delta$ . The larger the  $x$  is, the higher the spectral resolution is. To reduce  $x$  and get a bright spectral image,  $f$  and  $\Delta$  should, respectively, be short and wide.

However, it is not easy designing a spectral camera with a collimator where  $f$  is short enough. Commercially available gratings have more than 300 grooves per mm, that is  $\Delta$  is smaller than 3.3  $\mu\text{m}$ . Then,  $f$  must be shorter than 5 mm to make  $x = 1$  mm, roughly one-tenth of our image sensor's size, at  $\lambda = 660$  nm. At the same time, the lens's aperture must be larger than the size of the image sensor (e.g., 10 mm) to obtain a large field of

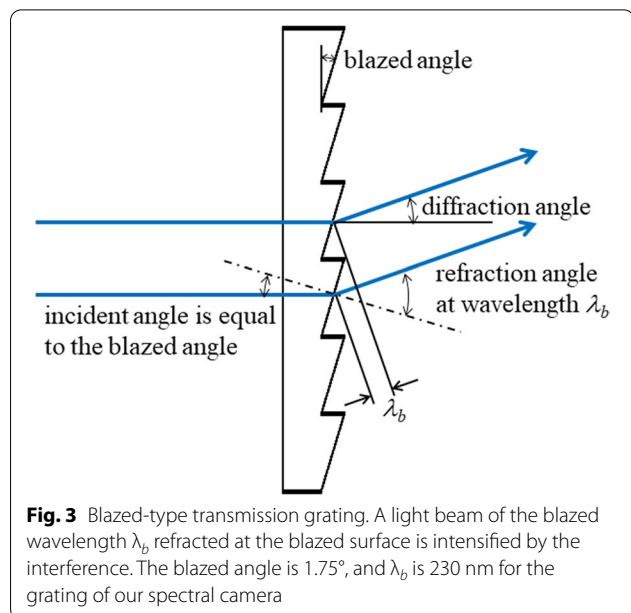
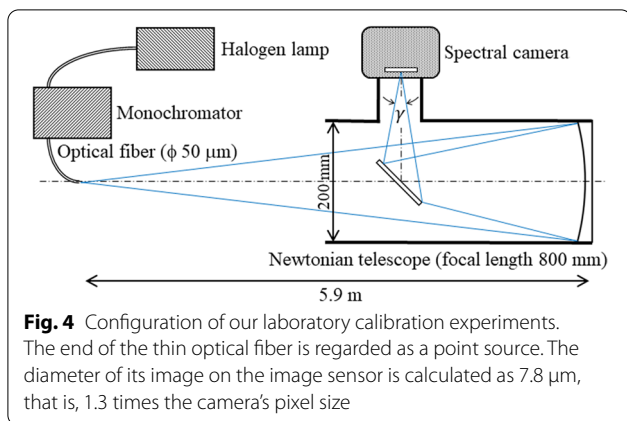


**Fig. 3** Blazed-type transmission grating. A light beam of the blazed wavelength  $\lambda_b$  refracted at the blazed surface is intensified by the interference. The blazed angle is 1.75°, and  $\lambda_b$  is 230 nm for the grating of our spectral camera

view. However, there is no lens of 5 mm in focal length and 10 mm in aperture.

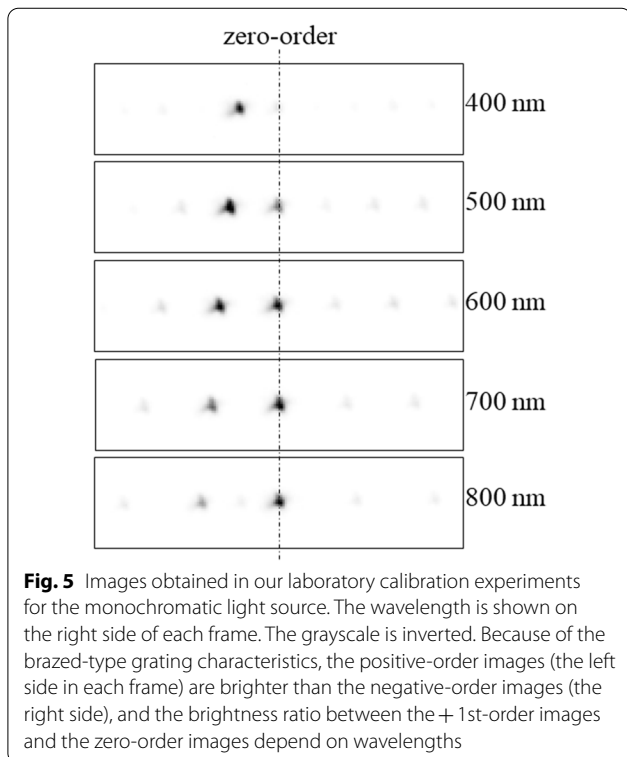
The converging light from our Newton reflector 450 mm in aperture and 2025 mm in focal length (Fig. 2) directly enters the gratings, passes through them, and is focused on the image plane of a silicon image sensor (the inset in Fig. 2). The no-collimator is not a standard way to use gratings, but works for low-resolution spectroscopies. The image sensor and electronics, which we call “camera,” are an ASI174MM manufactured by the ZWO company. This camera does not have a cooling system to reduce image noise. We removed the camera's cover glass and glued a blazed-type grating on the cover glass of a CMOS image sensor (SONY IMX174MM) with optical grease.

We used the grating of the widest groove spacing  $\Delta$ , which is commercially available. The grating has 70 grooves per mm ( $\Delta = 14 \mu\text{m}$ ) and is sold as “Transmission Grating Beamsplitters” by Edmund Optics. The brightness ratio of the 1st- to the zero-order image is maximum at the blaze wavelength in blazed-type gratings (Fig. 3). This is because the direction of a light beam refracted at the grooved surface is equal to that of the 1st-order light beam at the blaze wavelength. Our grating designed as a beam-splitter divides a laser beam of 633 nm in wavelength into a zero-order beam and a 1st-order beam evenly. It should be noted that the blaze wavelength is not 633 nm but 230 nm. Therefore, the grating is not efficient in obtaining spectral images in visible and near-infrared wavelengths. Gratings with the blaze wavelength in the visible and near-infrared range and a large groove spacing, if available, would increase the performance of the spectral observations.



The image sensor's pixel size is  $5.86 \times 5.86\ \mu\text{m}$ , and its resolution,  $1936 \times 1216$  pixels, makes its frame size  $11.3 \times 7.13\ \text{mm}$ . Its field of view is  $19.2 \times 12.1$  arc-minutes when it is attached to the telescope. In our observations, the field of view corresponds to  $2070 \times 1300\ \text{km}$  on the lunar disk at a distance of about  $3.7 \times 10^5\ \text{km}$ .

The camera's exposure time was set to 12.5 ms, 16.7 ms, or 20.0 ms in the observations. The electrical gain of the camera was set to 35 dB or 40 dB. Inter-frame durations



are negligible (e.g., 0.1 ms in our observations with the 20.0 ms exposure time). Therefore, the frame interval was almost the same as the exposure time.

We connected the camera to a personal computer with a USB3.0 cable. An application, "Fire Capture 2.4 (Fire-Capture 2021)" was used for capturing videos in the 16bit SER format. The bit depth of the camera signal is 12 bits in the no-binning mode and 14 bits in the  $2 \times 2$  binning mode. The videos were stored on a hard disk drive.

## Laboratory calibration of the spectral camera

### Wavelength calibration

We examined how the distance of the 1st-order image from the zero-order image depends on wavelength in a configuration illustrated in Fig. 4. One of the ends of a quartz optical fiber of  $50\ \mu\text{m}$  in core diameter is regarded

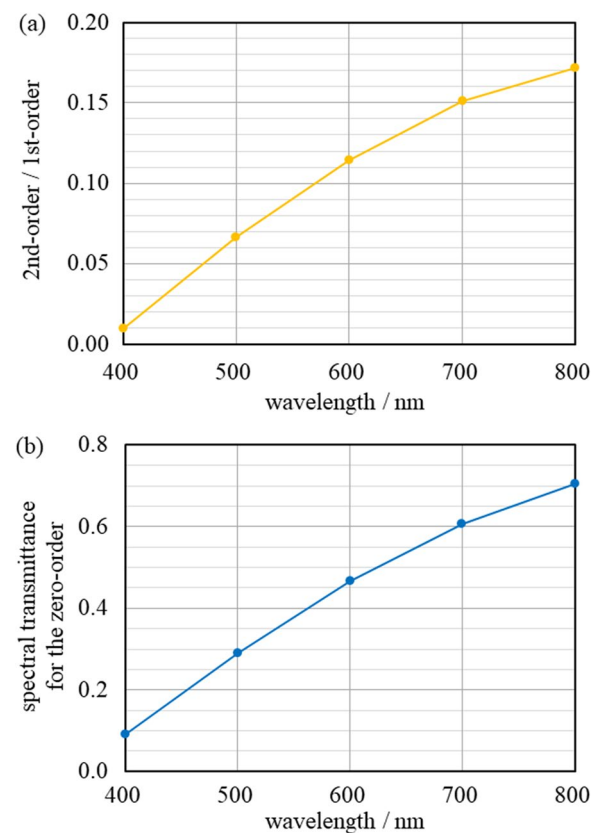


**Fig. 6** **a** The brightness ratio of the 2nd-order to the 1st-order images is plotted against wavelength. The ratios were measured in laboratory calibrations and are used in the correction for the 2nd-order image. **b** The brightness fraction of the zero-order image in the zero-, 1st-, and 2nd-order images. The contribution of the other order images is negligible. The fraction is equivalent to the relative transmittance of the grating for the zero-order if the other factors that reduce lights (e.g., absorptions in the glass) are independent of wavelengths. For the calculations in Eq. (2), the fraction was assumed to be constant at 800 nm and more



as a point source. The converging angle of rays at the image plane  $\gamma$  may affect the dependence. The angle is  $13^\circ$  when we attach the camera to the 450 mm telescope. In the configuration in Fig. 4, the angle is  $12^\circ$ ; that is, it reproduces the paths of light rays that enter the camera in the observations. The results of the experiment (Fig. 5)

show that the distance  $x$  is proportional to the wavelength  $\lambda$  in the range of 400–800 nm as

$$\lambda = ax, \quad (1)$$

where  $a = 23.9 \text{ nm pixel}^{-1}$  if we measure the distance in pixel ( $5.86 \mu\text{m}$ ).

Similar experiments using a commercial camera lens of 50 mm in focal length instead of the Newtonian telescope show the same relationship. First, a collimator converted the diverging light from the optical fiber's end to a parallel beam. Then, the parallel beam enters the camera lens in the experiments. The converging angle was kept to about  $13^\circ$ .

We examined the relationship only for the images that appear roughly around the center of video frames. We did not deliberately check whether the relationship depends on the images' position in a frame or not. However, many experiments by some students show the same result. Therefore, we conclude that the relationship holds regardless of wherever the images appear in a frame.

### Higher-order images

There appeared 2nd-order images as well as the zero- and the 1st-order images in the experiments (Fig. 5). The 3rd- and higher-order images and the negative-order images corresponding to downward output direction in Fig. 3 are also recognized. However, they are much less intense than the zero-, 1st-, and 2nd-order intensities. Figure 6a shows the intensity ratio of the 2nd- to the 1st-order images as a function of wavelength. We use the relationship to subtract the contamination of the 2nd-order

**Table 1** Summary of observations

Year/month/day (UT)	Observation time [hour]	Moon age <sup>a</sup>
2016/10/24	1.5	23 <sup>b</sup>
11/03	0.5	4
11/05	2.0	6
11/07	2.7	8
12/06	4.0	7
12/07	1.5	8
2017/01/01	0.3	3
01/03	3.0	5
01/05	4.9	7
01/31	1.2	3
02/01	2.3	4
02/02	2.5	5
02/03	3.7	6
02/04	4.9	7
05/01	2.6	5
05/02	2.8	6
Total	40.4 (16 nights)	

<sup>a</sup> The age of the Moon at 10:00 (UT)

<sup>b</sup> An observation made exceptionally during the waning crescent

**Table 2** Candidates of lunar impact flashes

Flash <sup>a</sup>	Time (UT) <sup>b</sup>	Latitude <sup>c</sup> [degree]	Longitude <sup>c</sup> [degree]	Number of frames <sup>d</sup>	Exposure <sup>f</sup> [ms]	Gain <sup>f</sup> [dB]	Binning
161107	10 h 15 m 54 s	21	− 64	1 or 2 <sup>e</sup>	16.7	35	no
170201	10 h 05 m 37 s	22	− 38	4	20.0	40	2 × 2
170204a	09 h 41 m 38 s	7	− 48	1	20.0	40	2 × 2
170204b	12 h 29 m 32 s	23	− 31	1	20.0	40	2 × 2
170204c	13 h 14 m 44 s	− 10	− 32	1	20.0	40	2 × 2
170204d	13 h 20 m 11 s	34	− 73	3	20.0	40	2 × 2
170501	10 h 43 m 02 s	8	− 78	2	20.0	40	2 × 2
170502a	11 h 20 m 05 s	− 22	− 28	1	20.0	35	2 × 2
170502b	11 h 57 m 53 s	25	− 40	1	12.5	40	2 × 2
170502c	12 h 15 m 39 s	44	− 30	1	20.0	40	2 × 2

<sup>a</sup> Flashes are named after dates. A flash observed on Nov. 7, 2016 (UT) is named "161107"

<sup>b</sup> The times of detections. They are accurate to a second

<sup>c</sup> Selenographic latitudes and east longitudes in degree. They are accurate to a degree except for the longitudes of Flashes 170204d and 170501

<sup>d</sup> The number of frames where each flash is recognized by visual inspection

<sup>e</sup> There may be a frame that shows the flash if the frame drops had not occurred. See text

<sup>f</sup> The exposure time for a frame and the electrical gain of the camera

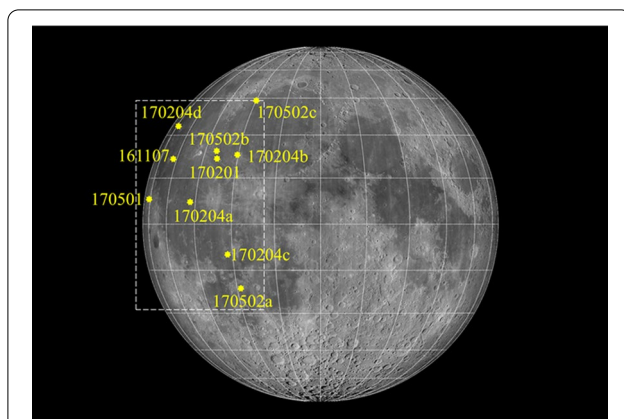


**Fig. 7** Locations of the ten lunar impact flash candidates. They were observed at the University of Electro-Communications (UEC) in Tokyo, Japan. The candidates are named after dates, e.g., one observed on Nov. 7, 2016 (UT) is named “161107”. The dashed rectangular shows the size and the approximate position of the field of view in our observations. The lunar image was obtained by using the Virtual Moon Atlas (2021)

images. The zero-order intensity ratio in the sum of the zero-, 1st-, and 2nd-order intensities is shown in Fig. 6b. We use the relationship later in the correction for the atmospheric dispersions.

We obtained Fig. 6a and b for the images around the center of a frame. The ratios in the figures may depend on the image positions in a frame. However, the dependence would not significantly affect our results because we use the relationships for generally slight corrections.

## Observations and interpretations

### Observations

We made observations at the University of Electro-Communications (UEC) in Tokyo, Japan (35° 39′ 28″ N in latitude, 139° 32′ 37″ E in longitude, and 80 m in elevation). The telescope pointed to the night-side of the Moon during the waxing crescent in Nov. 2016–May 2017 (Table 1). No observation was made in March and April due to cloudy skies. After the observations on each night, an application, “ser\_scan,” developed by us (Yanagisawa and Kakinuma 2022), scanned the SER videos. This application searches for pixels whose brightness exceeds  $n\sigma$ , where  $\sigma$  is the background fluctuation and  $n$  is a preset value of about 6. As a result, we found ten flashes (Table 2, Fig. 7). An Additional file 1 shows the video of Flash 170201 observed on Feb. 1, 2017 (UT).

All the flashes except Flash 161107 were detected in the latter half of the 40.4 h of observation in total. In the first half of our observation period, we could fail to detect flashes, probably due to the frame drops described later because we did not use the binning mode constantly.

Despite no direct sunlight illumination, we can recognize the bright Aristarchus region and the dark Grimaldi crater on the night-side images of the Moon illuminated by the Earth (earthshine). First, we assume that all the flashes were lunar phenomena. Then, based on the flashes’ positions relative to Aristarchus and Grimaldi, we determined their selenographic latitudes and longitudes on the maps generated by an application “Virtual Moon Atlas (2021).”

“Fire Capture (2021)” outputs computer clock times for all frames in a video as a text file. Therefore, we can determine the times at the appearances of the flashes (Table 2). The accuracy of the times is  $\pm 1$  s because the computer clock was adjusted manually.

The intervals of the recorded times should be constant and almost the same as the exposure time if there is no frame drop (see Paper I for details). The frame drops occur when image data transferred through the USB3.0 cable and stored into the disk exceeds the computer system’s capability. We examined the recorded times and found that a frame was missed just before or after the frame of Flash 161107. The camera was set to the no-binning mode that night. The amount of image dataflow must be too much to be transferred and stored stably. There was no frame drop for the other flashes.

### Possibility of artificial satellites’ glints

The existence of both the zero-order and spectral images rules out the possibility of electric noise and cosmic ray hits for the observed flashes. Then, the most significant source of the false-positive detections of lunar impact flashes is the reflection of sunlight by artificial satellites or space debris. The best way to distinguish the lunar flashes from the satellite glints is by examining the videos obtained at least two observatories separated far enough. Unfortunately, there is no other simultaneous observation for these flashes.

Therefore, we examined the possibility of satellites’ glints by two methods. First, we examined whether cataloged satellites or space debris passed in front of the lunar disk accidentally. We downloaded the orbital datasets (two-line elements) of the 13,000–19,000 satellites or space debris from “Space-Track (2021)” within 5 days of each observation. Then, we examined whether any object appeared on the celestial sphere within a circle centered at the Moon of 1° in radius, within  $\pm 1$  min of the time of each flash, using an application “Stella-Navigator 10 (2021)” by the Astro Arts company. We found two objects in total. However, they move relative to the Moon more than 500 arcseconds  $s^{-1}$ . This angular velocity is large enough to make satellite images

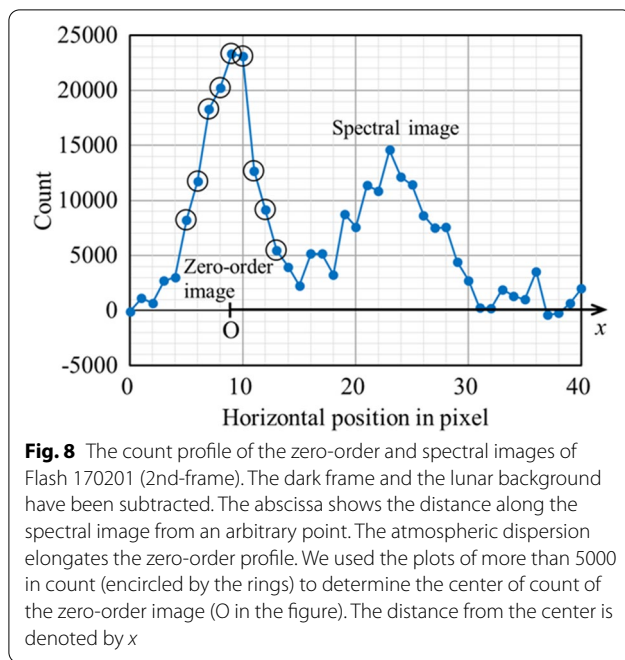


**Fig. 8** The count profile of the zero-order and spectral images of Flash 170201 (2nd-frame). The dark frame and the lunar background have been subtracted. The abscissa shows the distance along the spectral image from an arbitrary point. The atmospheric dispersion elongates the zero-order profile. We used the plots of more than 5000 in count (encircled by the rings) to determine the center of count of the zero-order image (O in the figure). The distance from the center is denoted by  $x$

elongated by motion blur, unlike lunar flash images. Therefore, the cataloged objects are not the sources of the flashes we detected.

Second, we monitored the sky close to the belt of geostationary satellites on the celestial sphere for 7.5 h in total. We scanned the recorded videos by the “ser\_scan” (Yanagisawa and Kakinuma 2022). No flash as we observed on the lunar disk was detected. On the other hand, we detected four flashes in our 4.9-h observations on Feb. 4, 2017, and three flashes in 2.8 h on May 2, 2017 (Table 1). We may say that almost all the flashes we observed would be lunar impact flashes though there could be a small probability of satellites’ or space debris’ glints.

### Spectral analyses

First, we prepared a dark frame for each observation by averaging SER format video frames obtained without light inputs. Second, the dark frames were subtracted from all SER video frames, including flashes and stars.

We prepared a lunar background frame for each flash by averaging SER video frames after the dark frame correction. Then, the background frame was subtracted from frames that included flash images after the dark frame correction.

In the analyses of stellar images, we averaged SER video frames after the dark frame correction. The averaging increases the signal-to-noise ratio of the spectral images.

Examples of raw SER videos are in Additional file 4. Software tools developed by us for processing SER videos are in Additional files 5, 6, 7, 8.

The spectral dispersion direction of our camera is horizontal in images. Therefore, we summed pixel values of the zero-order and spectral images over some pixels along a vertical column. We thus obtained the summed count as a function of horizontal position, as illustrated in Fig. 8. We used EXCEL to calculate the sum (e.g., Additional file 9).

### Corrections for the atmospheric dispersion

Light rays from a star are bent due to atmospheric refraction. Wavelength dependence of the refraction angle makes blue image up and red image down relatively and leads to a vertically elongated image of the star (Fig. 9a). If it were not for the atmosphere, spectral dispersion by a grating would make a point image for the zero-order and a straight-line image for the 1st- and higher orders. The wavelength dependence distorts both the zero-order and the spectral images.

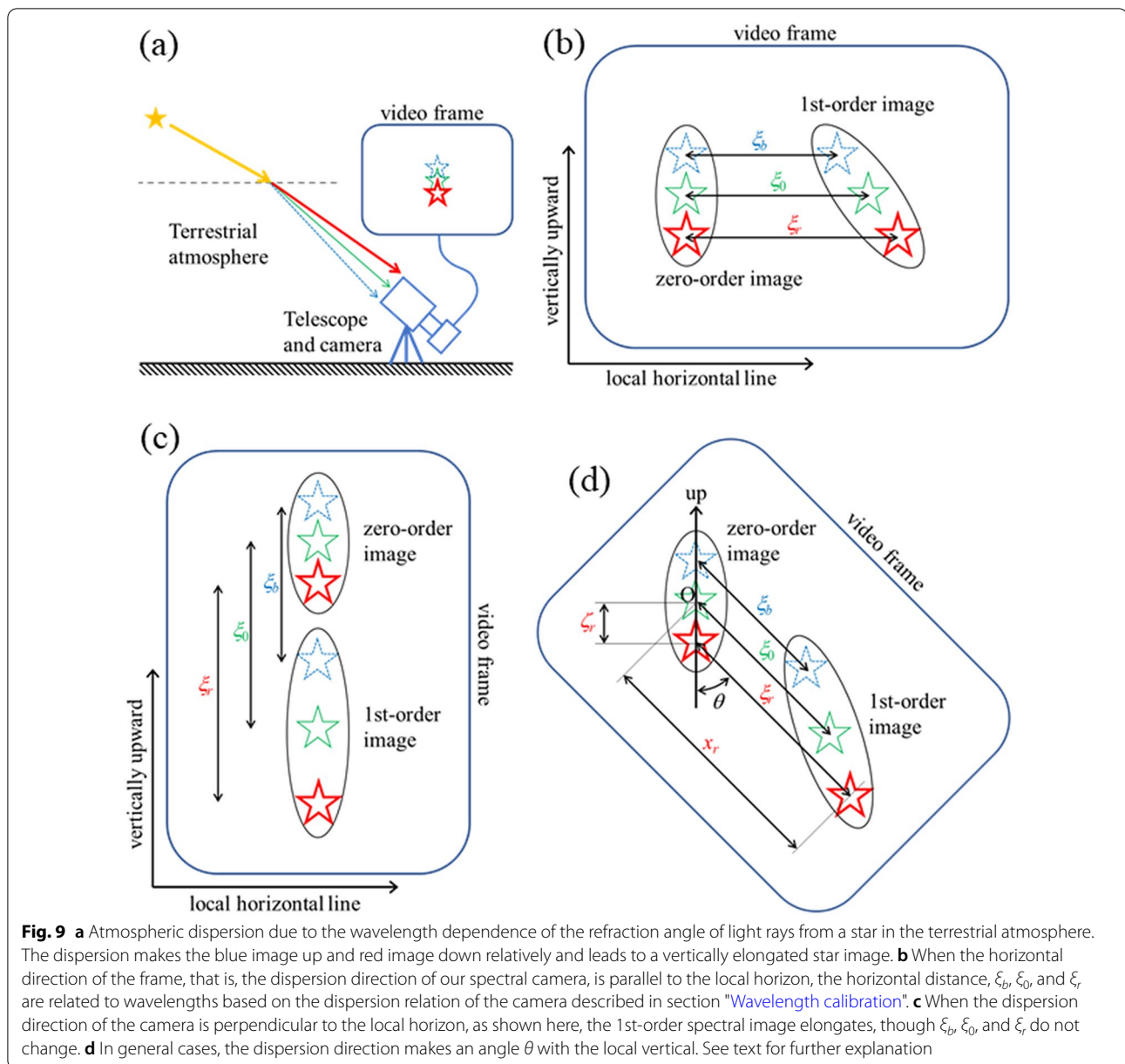
If the dispersion direction by the grating is parallel to the local horizon, blue components of a stellar image shift up, and red components shift down due to the atmospheric dispersion (Fig. 9b). Then, the zero-order image slightly elongates vertically, and the spectral image bends a little (e.g., Fig. 10a). On the other hand, if the dispersion direction is locally downward, the spectral image elongates (e.g., Figs. 9c and 10b). The dispersion direction generally makes an angle  $\theta$  with the local vertical, as shown in Fig. 9d.

The spectral resolution of our camera is pretty low, and the spectral image is not much longer than the elongation of a point source image by the atmospheric dispersion. Furthermore, we observe the Moon when its elevation is not high, and the dispersion is significant. Therefore, the correction for the dispersion is essential. Fortunately, the atmospheric refraction is well formulated as a function of wavelength and zenith angle (Schubert and Walterscheid 1999).

First, we obtained the center of count (brightness) of the elongated zero-order image profile, similar to obtaining a center of mass. It is about 9 in the horizontal position in Fig. 8 and is denoted by O in Figs. 8 and 9d. We calculated the atmospheric refraction angle corresponding to the center of count as follows:

$$\alpha_0 = \frac{\int \alpha(\lambda) F(\lambda) s(\lambda) T_r(\lambda) d\lambda}{\int F(\lambda) s(\lambda) T_r(\lambda) d\lambda}, \quad (2)$$

where  $\lambda$  denotes a wavelength,  $F(\lambda)$  is the spectral form of a star,  $\alpha(\lambda)$  is the atmospheric refraction angle at the star’s zenith angle,  $s(\lambda)$  is the sensitivity of our observation system, and  $T_r(\lambda)$  is the atmospheric transmittance



at the star's zenith angle. The spectral form was approximated by a blackbody spectrum of the effective temperature of the star. For the flashes, we adopted the spectrum of 3000 K at first. As shown later, best-fitted blackbody spectra to the spectra obtained as results show this temperature for most of the flashes. The spectra of Flashes 170204a, 170204c, and 170502b were quite different from the 3000 K blackbody spectrum. The best-fitted blackbody spectra corresponded, respectively, to 7000 K, 7000 K, and 11,000 K. We changed  $F(\lambda)$  to the blackbody spectral forms at these temperatures and re-calculated  $\alpha_0$  for them. The refraction angle  $\alpha(\lambda)$  was calculated from

the formulae in Schubert and Walterscheid (1999). In the calculation, we set the surface temperature, pressure, and water vapor partial pressure, respectively, to 288 K,  $1.013 \times 10^5$  Pa, and 550 Pa. The sensitivity includes the spectral sensitivity of the image sensor and the spectral throughput of the grating for the zero-order image (Fig. 6b). The atmospheric transmittance was obtained from a free web application of MODTRAN (MODTRAN 2021), as described later. Once we obtain  $\alpha_0$ , it is converted to the wavelength  $\lambda_0$  by the formulae in Schubert and Walterscheid (1999).  $\lambda_0$  corresponds to the center of count of the zero-order image. The integrations in Eq. (2)



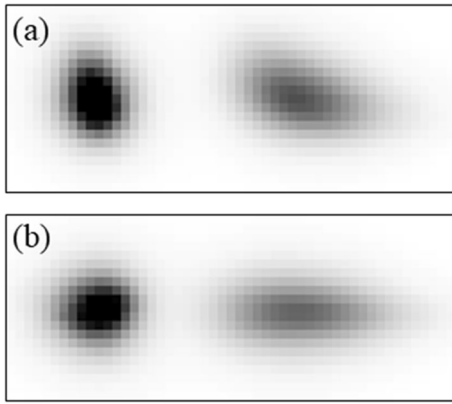


**Fig. 10** Zero-order (left) and spectral (right) images of  $\beta$  Cet (Diphda, 2nd in V-magnitude) observed by our spectral camera and the telescope on Nov. 9, 2017. One hundred frames were averaged, and the grayscale is inverted. We flipped the frames horizontally to show the spectral image right side of the zero-order image. The star was around a meridian transit at  $54^\circ$  in zenith angle. **a** The zenith is up in the image, corresponding to Fig. 9b. **b** We rotated the camera, and the zenith is the left-hand side, corresponding to Fig. 9c

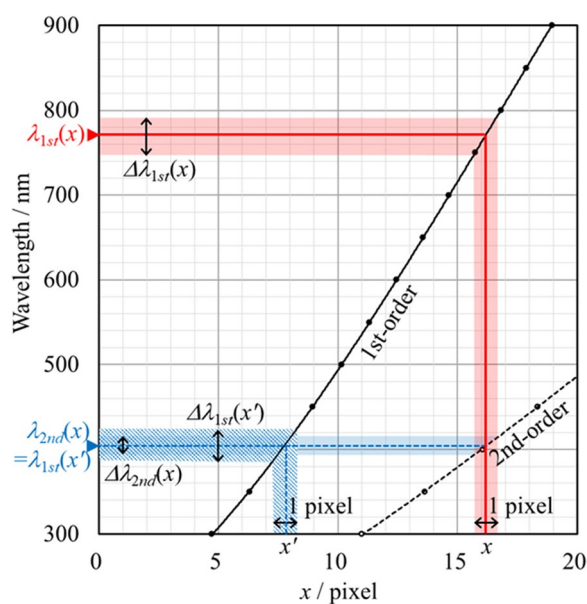


**Fig. 11** The relationship between the distance from the center of count in Fig. 8 and wavelengths for the 1st- (solid line) and 2nd-order (broken line) spectral images. Because of the atmospheric dispersion, the relationships are non-linear. Therefore, cubic polynomial lines were best fitted to the plots. See text for details

were made numerically between 400 and 1000 nm with  $d\lambda = 100$  nm.

The distance from the center of count in a count profile ( $x$  in Fig. 8) corresponds to a wavelength as

$$x = \varsigma \cdot \cos\theta + \xi, \quad (3)$$

where

$$\varsigma = -[\alpha(\lambda) - \alpha_0]/b, \quad (4)$$

$$\xi = \lambda/a \quad (\text{see Eq. (1) for the constant } a). \quad (5)$$

The angular field of view for a pixel is denoted by  $b$ . It is  $0.597 \text{ arcsec pixel}^{-1}$  in the no-binning mode. For red lights  $\alpha(\lambda) < \alpha_0$ , then  $\varsigma$  is positive. These equations give us  $x$  as a function of  $\lambda$ . We calculated the values of  $x$  for  $\lambda$  between 300 and 1000 nm with a 50 nm step (Fig. 11). We then obtained a cubic polynomial function  $\lambda_{1st}(x)$ , the wavelength for the 1st-order spectral image as a function of  $x$ , by fitting the function to the plots. The function gives us the 1st-order wavelength for each plot in Fig. 8. Just by replacing  $a$  in Eq. (5) by  $2a$ , a function that gives us the 2nd-order wavelength  $\lambda_{2nd}(x)$  was obtained in the same way.

The wavelength width for each plot in Fig. 8 is expressed as:

$$\Delta\lambda_{1st}(x) = (d\lambda_{1st}(x)/dx) \cdot 1\text{pixel}. \quad (6)$$

We use the width in converting the flux for a plot in a count profile to the flux per unit wavelength. Similarly, the plot is contaminated by the 2nd-order light at  $\lambda_{2nd}(x)$  with the following wavelength width:

$$\Delta\lambda_{2nd}(x) = (d\lambda_{2nd}(x)/dx) \cdot 1\text{pixel}. \quad (7)$$

We made calculations on Eqs. (3)–(7) by EXCEL (Additional file 9).

#### Corrections for the 2nd-order image

The count  $C(x)$  for a plot at  $x$  for a spectral image in Fig. 8 consists of  $C_{1st}(x)$  of the 1st-order light at  $\lambda_{1st}(x)$  and  $C_{2nd}(x)$  of the 2nd-order light at  $\lambda_{2nd}(x)$ , that is,

$$C(x) = C_{1st}(x) + C_{2nd}(x). \quad (8)$$

We extract  $C_{1st}(x)$  and obtain the count per unit wavelength at  $\lambda_{1st}(x)$  as,

$$N(\lambda_{1st}(x)) = C_{1st}(x)/\Delta\lambda_{1st}(x). \quad (9)$$

The procedure is illustrated in Fig. 11.

The light of the wavelength  $\lambda_{2nd}(x)$  makes the 2nd-order image at  $x$  and the 1st-order image at  $x'$ . Therefore,

$$\lambda_{2nd}(x) = \lambda_{1st}(x'). \quad (10)$$

The wavelength that generates the 2nd-order count at  $x'$ , which is roughly  $\lambda_{1st}(x')/2$ , is out of the wavelength range where the camera has the sensitivity. Therefore, the count

**Table 3** Comparison stars for deriving flash spectra

Flashes	Tycho-2 catalog No	Spectral type	B-magnitude	V-magnitude	Effective temperature <sup>a</sup> /K
161107	1735-3180-1	B8IV	1.95	2.06	12008
170201	4665-715-1	F2V	9.00	8.60	6725
170204a	651-1202-1	K5 <sup>b</sup>	10.61 <sup>b</sup>	9.45 <sup>b</sup>	4553
170204b	652-390-1	F8	10.08	9.47	5855
170204c and d	652-379-1	F5	7.80	7.35	6496
170501	1351-474-1	G5	9.81	8.84	4902
170502a	1378-835-1	A0	6.96	7.00	10195
170502b	1378-563-1	K0	7.84	6.66	4518

Spectral types and magnitudes are obtained from the SIMBAD (2021) database

<sup>a</sup> Effective temperatures are obtained from B–V color indexes according to Table 3 in Flower (1996)

<sup>b</sup> The type and magnitudes could be slightly modified by the recent update

at  $\lambda_{1st}(x')$ ,  $C_{1st}(x')$  is not contaminated by 2nd-order lights.

The light of count per unit wavelength  $C_{1st}(x')/\Delta\lambda_{1st}(x')$  at  $\lambda_{1st}(x')$  generates the 2nd-order light of count per unit wavelength  $[C_{1st}(x')/\Delta\lambda_{1st}(x')] \cdot r(\lambda_{1st}(x'))$  at  $x$ . Here,  $r(\lambda)$  denotes the ratio of the 2nd-order to the 1st-order counts at  $\lambda$  shown in Fig. 6a. The 2nd-order light contributes to  $C(x)$  by

$$C_{2nd}(x) = [C_{1st}(x')/\Delta\lambda_{1st}(x')] \cdot r(\lambda_{1st}(x')) \cdot \Delta\lambda_{2nd}(x). \quad (11)$$

Then, the count per unit wavelength at  $\lambda_{1st}(x)$  is obtained as

$$N(\lambda_{1st}(x)) = [C(x) - C_{2nd}(x)]/\Delta\lambda_{1st}(x). \quad (12)$$

Because  $x'$  usually does not correspond to any plot in Fig. 8, we obtained  $C_{1st}(x')$  by the interpolation from the two adjacent plots. The subtraction of  $C_{2nd}(x)$  in Eq. (12) was made only when it was positive. The contributions of the higher-order lights are negligible, and we did not correct them. We made the corrections for the 2nd-order image by EXCEL (Additional file 9).

is different between them, and we made corrections to the count  $N(\lambda)$  as

$$N(\lambda) \cdot T_r(\lambda)^{-1/\cos\vartheta} \quad (13)$$

to obtain the count without the atmospheric absorption, where  $\vartheta$  denotes the zenithal angle of a flash or a star.

We obtained the zenithal atmospheric transmittance as a function of wavelength  $T_r(\lambda)$  between 400 and 1000 nm with the following three parameters using a free web application of MODTRAN (2021); summer, mid-latitude, and urban. The temperature in Tokyo (Japan) is not so cold as in typical mid-latitude countries, even in winter. We adopted “summer” therefore instead of “winter” as a parameter though we did not observe in summer (Table 1). The transmittance between 300 and 400 nm was obtained from Table 11.25 in Schubert and Walterscheid (1999). We assume no difference in atmospheric conditions, such as water vapor and aerosol contents, among observations.

### Comparison stars

The spectral flux densities  $\bar{F}_{flash}(\lambda)$  at wavelength  $\lambda = \lambda_{1st}(x)$  of a flash is calculated as

$$\bar{F}_{flash}(\lambda) = \frac{N_{flash}(\lambda) \cdot T_r(\lambda)^{-1/\cos\vartheta_{flash}}}{N_{star}(\lambda) \cdot T_r(\lambda)^{-1/\cos\vartheta_{star}}} \cdot \left[ \frac{N_{\alpha And_{star}}(\lambda)}{N_{\alpha And_{flash}}(\lambda)} \right] \cdot k \cdot \pi B_{T_{star}}(\lambda), \quad (14)$$

### Corrections for the atmospheric transmittance

As described in the following section, we compare the count profiles of a flash and a comparison star to derive the flash spectrum. The flash and the star are usually observed independently at different times and in different directions. Therefore, the atmospheric transmittance

where  $N_{flash}(\lambda)$  and  $N_{star}(\lambda)$  are count numbers obtained by Eq. (12). Their subscripts represent a flash and a comparison star. If the gain and the exposure time of the camera are different between the flash and the star, we made corrections for the differences before applying Eq. (14). Their zenithal angles are denoted by  $\vartheta_{flash}$  and  $\vartheta_{star}$ . The item in the square brackets is the correction for the spectral flat-field described in the next section.

$B_{T_{star}}(\lambda)$  represents the Planck function at temperature  $T_{star}$ . For the  $T_{star}$ , we used the effective temperature of the star derived from its color index,  $B-V$ , and Table 3 in Flower (1996). We obtained the B- and V-magnitudes ( $B$  and  $V$ ) from the SIMBAD (2021) database. Characteristics of comparison stars used for each flash are summarized in Table 3.

A non-dimensional value  $k$  in Eq. (14) related to the brightness of the comparison star is derived as follows:

$$k = k_{sun} \cdot \frac{\int \pi B_{T_{sun}}(\lambda) \cdot R_V(\lambda) d\lambda}{\int \pi B_{T_{star}}(\lambda) \cdot R_V(\lambda) d\lambda} \cdot 10^{-(V-V_{sun})/2.5}, \quad (15)$$

where

$$k_{sun} = \frac{C_{sun}}{(\sigma T_{sun}^4)}. \quad (16)$$

The response function for the V-band (Bessell 2005) is denoted by  $R_V(\lambda)$ . For the sun,  $V_{sun}$  is its V-magnitude of  $-26.75$  and  $T_{sun}$  is its effective temperature of  $5777$  K. The solar constant of  $1370 \text{ W m}^{-2}$  is denoted by  $C_{sun}$ .

We put a bar above  $F_{flash}(\lambda)$  to emphasize that  $\bar{F}_{flash}(\lambda)$  is a temporal average of the flux over the exposure time of the camera (Table 2). Six in ten flashes in Table 2 are recognized only in a frame, and their duration would be shorter than the exposure time. Even for the other flashes, the time constant of their brightness and spectrum variations would be shorter than the exposure time.

We did not intend to observe photometric-standard stars, but observed stars close to the Moon if they were bright enough. For each flash, we selected a star observed temporally close to the flash as a comparison star (Table 3). Of course, the flashes and the corresponding comparison stars were observed on the same night except for Flash 161107. Unfortunately, a star we observed on Nov. 7, 2016, is an M2-type giant. The spectra of M-type stars are not approximated well by the Planck function. Therefore, we used  $\alpha$  And (TYC1735-3180-1) observed on Nov. 9, 2017, as a comparison star for the flash.

We derived spectra of the stars in Table 3 with similar methods as the analyses for the flashes by using  $\alpha$  And as the comparison star (Additional file 2). Their V-magnitudes were calculated from the observed spectra. Blackbody spectra were best fitted to them, and the temperatures of blackbodies are shown in these figures. The V-magnitudes are smaller (brighter) than the values in Table 3, but agree to them within 0.6. The temperatures are higher than those in the table, but agree to them within 12%, except TYC652-390-1. These results would indicate that the uncertainties of the magnitudes and the temperatures we show later are, respectively, within 0.6 and 12%.

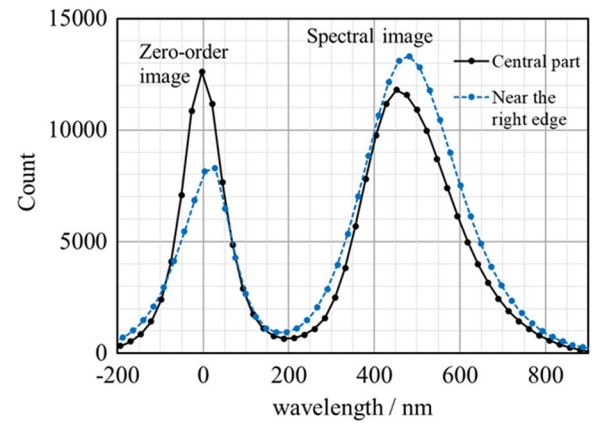


**Fig. 12** Count profiles of spectral images of a star,  $\alpha$  And (Alpheratz). The solid line profile was obtained for the star images that appeared in the video frames' central part (No. 5 in Fig. 14). The blue broken line profile was obtained for the images near the edge of the frames (No. 6 in Fig. 14). One hundred frames were averaged for each profile. We converted the positions in a spectral image to wavelengths and showed them in the abscissa. The dark frame has been subtracted. We did not apply the correction for the atmospheric dispersion because the star was close to the zenith. The correction for the 2nd-order images was made. We did not make the corrections for the atmospheric transmittance

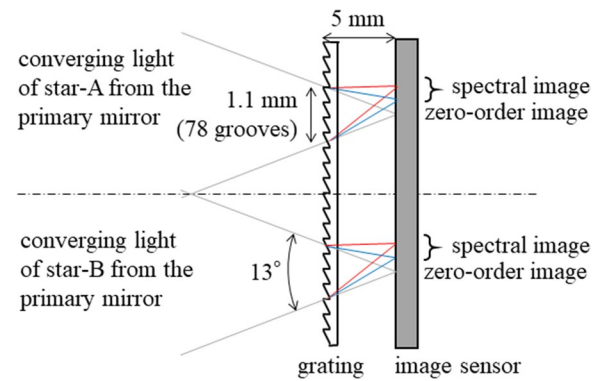
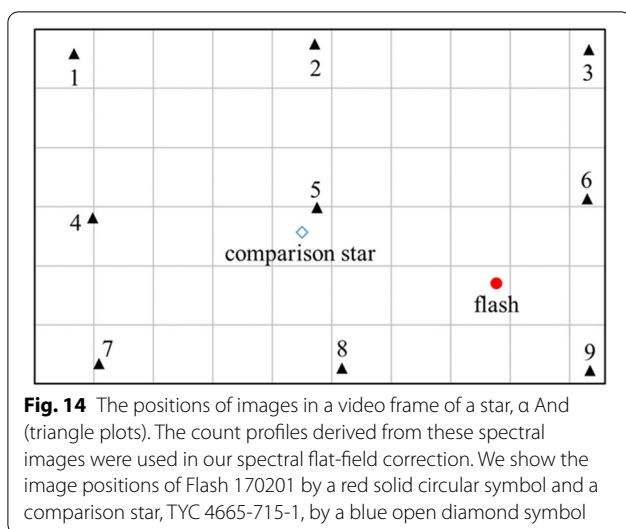


**Fig. 13** In our simple spectral camera, the converging light of a star passes the grating and focuses on the image sensor in our camera. The effective region of the grating depends on where the light focuses on the image sensor. The converging angle of  $13^\circ$  is calculated from the focal length and the aperture of our telescope

The best-fitted blackbody temperature for TYC652-390-1, the comparison star for Flash 170204b, is  $7600$  K, 30% higher than  $5855$  K estimated from  $B-V$  color index (Table 3). This star's spectrum may be approximated by a blackbody spectrum of the temperature higher than  $5855$  K; that is, we might underestimate the temperature of  $B_{T_{star}}(\lambda)$  in Eq. (14). Then, the derivation of the spectrum of Flash 170204b could lead to a redder spectrum than the real one.



### Spectral flat-field correction

One of the drawbacks of our spectral cameras is that the count profiles (e.g., Fig. 8) depend on where the spectral image appears in a frame. For example, a profile derived from images in the central part of a frame is different from that near the right edge in a frame (Fig. 12).

In spectral cameras with collimator lenses (Fig. 1), a light beam after the first lens is wide and passes almost the same grating area regardless of where a star image appears on the image sensor. On the other hand, in our camera, the area where the converging light passes is different depending on the image position on the sensor (Fig. 13). Therefore, slight non-uniformity of the grating or dirt on its surface could affect the spectral images. Besides, a small grating part, a circular area of 1.1 mm in diameter, contributes to the diffraction (Fig. 13). This part includes only 78 grooves. Therefore, if there are dust particles on the surface of this part, the spectral image could change.

The image position in video frames is different between a flash and a comparison star. Therefore, the dependence on the image position makes it difficult to derive a precise flash spectrum by comparing the count profiles between a flash and a comparison star without any correction. We call the correction “spectral flat-field correction” from now on.

Count profiles of a star were observed densely, along 20 horizontal lines over video frames, and used for the correction in Paper I. However, the non-uniformity and the dirt distribution over the grating could differ between the two observations due to our grating cleaning. Therefore, we do not use their data for the correction.

Instead, we observed a star,  $\alpha$  And (Alpheratz), on Nov. 9, 2017, at 9 points distributed uniformly in the field of

view (Fig. 14). The item in the square brackets in Eq. (14) corrects the non-uniformity of the spectral images. We explain it using Flash 170201 as an example.  $N_{\alpha And_{flash}}(\lambda)$  is the count profile of  $\alpha$  And observed at the closest point to the flash in a frame (No. 6 in Fig. 14).  $N_{\alpha And_{star}}(\lambda)$  is that at the closest point to the comparison star for the flash (No. 5 in Fig. 14). However, because the distribution of the  $\alpha$  And images is not dense, the correction could not be enough to derive accurate spectra. We show later how much the incomplete spectral flat-field correction affects our spectra in section “Effect of incomplete spectral flat-field correction”.

## Results

### Spectra

The spectral flux densities  $\bar{F}_{flash}(\lambda)$  of the flashes as are observed at the top of the terrestrial atmosphere are shown in Fig. 15. These spectra are reliable between 400 and 800 nm in wavelength. The analyses of the subsequent frames are possible for two flashes, and we also show their spectra. Flash 170502c appeared at the edge of a frame. Its spectral image was recorded, but only a part of the zero-order image was obtained. Therefore, it was impossible to determine the center of the zero-order image or the wavelengths for the positions on the spectral image. Therefore, a reliable spectrum was not obtained for the flash.

Error bars in the figures represent the temporal variation of the background. They include photon shot noise and electric noises. The same kinds of noise for the comparison stars are not considered because the averages of about one hundred frames reduce the noises. The effect of the atmospheric scintillation discussed later is not included in the error bars. We do not show error bars for the 2nd- and the 3rd-frames, but they are almost identical to the 1st-frame at the same wavelength.

Spectral flux densities in the wavelength range between 300 and 400 nm are inaccurate for the following reasons. First, the sensitivity of our spectral camera is low. Second, there could be some non-negligible absorptions in the stellar atmosphere in this range, and the blackbody approximations for the comparison stars could not be appropriate. Third, terrestrial atmospheric absorption is significant, 55% at 400 nm and 100% at 300 nm in the zenithal direction (Schubert and Walterscheid 1999). The absorption increases in the non-zenithal directions. Thus, even a slight uncertainty in the correction for the atmospheric transmittance could lead to poor accuracy.

Spectral flux densities at wavelengths over 800 nm could also be inaccurate. First, the sensitivity of our spectral camera is low. Second, the correction for the 2nd-order image is not minor, especially for blue flashes and



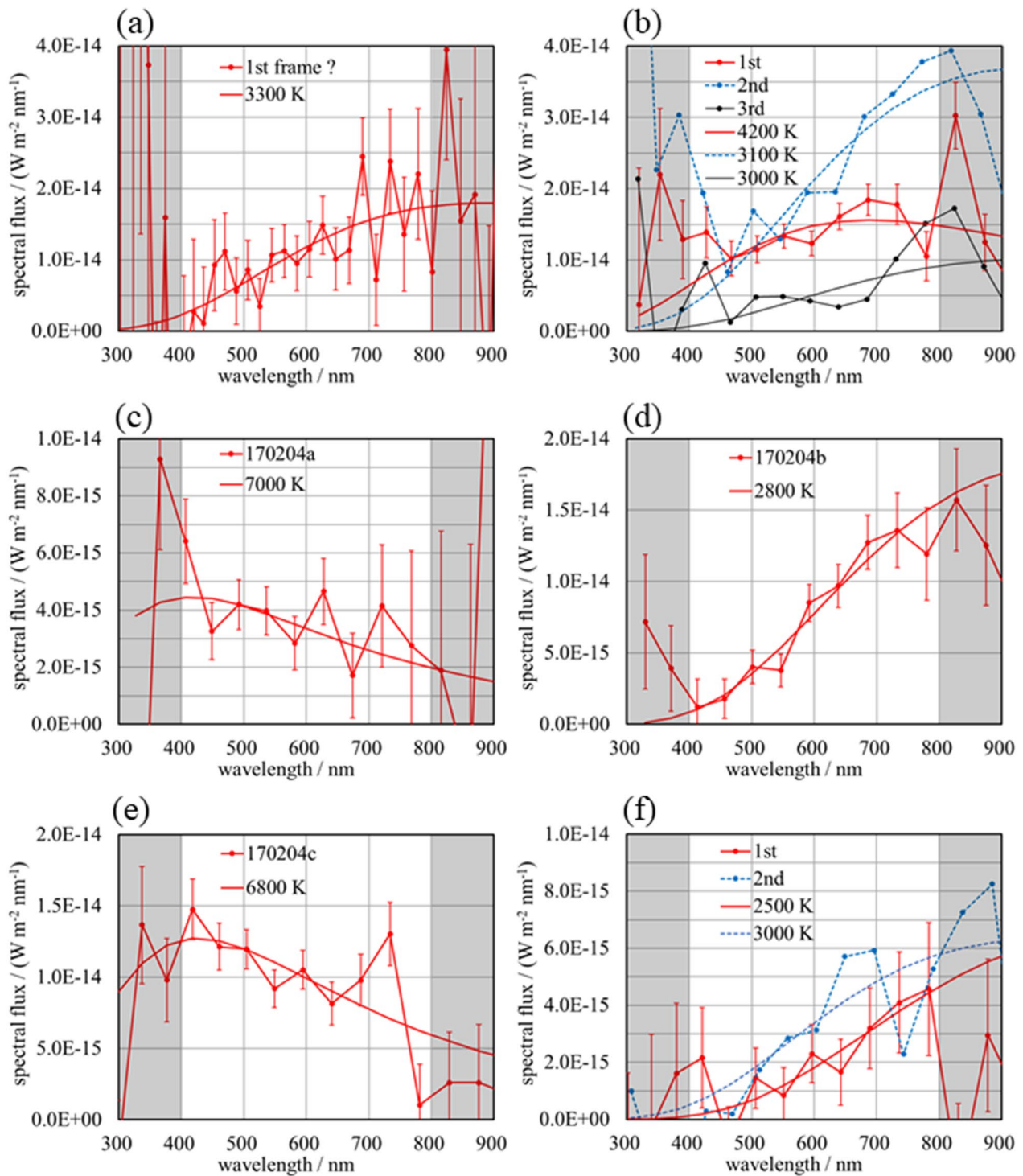


**Fig. 15** Spectra of the flashes. Flash name is shown in each panel where only a single frame is bright enough to analyze. For the others: **a** 161107, **b** 170201, and **f** 170204d. Red solid polygonal lines show the spectra for the frames where the flashes first appeared. The blue broken polygonal lines and a black thin polygonal line show the spectra at the 2nd- and 3rd-frames, respectively. Error bars represent one standard deviation of the background fluctuation. We do not show error bars for the 2nd- and 3rd-frames, but they are almost identical to those in the 1st-frame. The fluxes are reliable between 400 and 800 nm in wavelength (the non-shaded area). Blackbody spectra were best fitted to the plots in the non-shaded area and are shown by smooth curves. We show the blackbody temperatures in each panel. The exposure times are equal to the frame intervals and are listed in Table 2

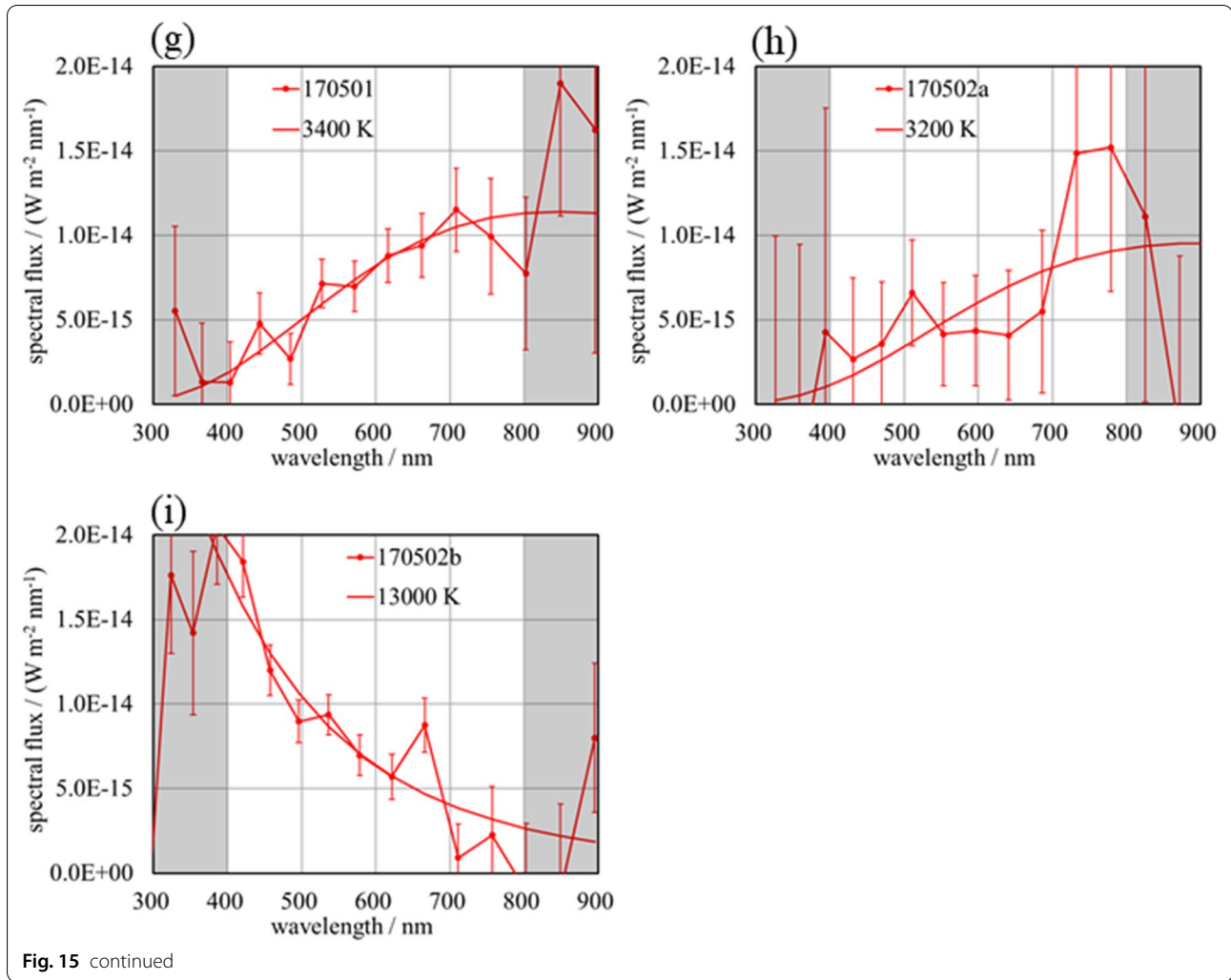


Fig. 15 continued

stars. The intense blue light of about 400 nm in wavelength, for example, contaminates the spectral image of 800 nm importantly. Though we corrected the 2nd-order image, the brightness ratio of the 2nd-order to the 1st-order images (Fig. 6a) used in the correction may depend on the image position in a frame. If so, the dependency would cause non-negligible errors.

draw it as a smooth line and show the blackbody temperature in each figure and Table 4. The plots in the reliable wavelength ranges, 400–800 nm, were used in the best-fittings.

#### Brightness magnitudes and meteoroid masses

The magnitudes  $m_{flash}$  were calculated according to the following formula for the V-, R-bands independently:

$$m_{flash} - m_{sun} = -2.5 \log_{10} \left[ \frac{\int \bar{F}_{flash}(\lambda) R(\lambda) d\lambda}{\int F_{sun}(\lambda) R(\lambda) d\lambda} \right], \quad (17)$$

Continuum spectra seem to dominate the spectra in Fig. 15. Emission lines or bands may also exist. However, the low spectral resolution and noise would make their existence unclear unless they are very intense. Though a single blackbody spectrum may not necessarily dominate the continuum, it was best fitted to each spectrum. We

where  $m_{sun}$  is the solar magnitude and  $R(\lambda)$  is the response function for the band (Bessell 2005). The integrals were calculated numerically, where we used the plot intervals in Fig. 15 as  $d\lambda$ . We did not truncate the integration at 800 nm for calculating the R-magnitude, though the spectrum could be inaccurate over the wavelength.

**Table 4** Summary of some parameters derived for the flashes

Flash	Blackbody temperature/K	V-magnitude	R-magnitude	Mass <sup>a</sup> /g	Effective diameter of radiating source <sup>b</sup> /m	Crater diameter/m
161107 <sup>c,d</sup>	3300	9.0	7.8	330	1.5	3.7
170201 <sup>e</sup>	4200	8.6	7.7	1300	0.72	5.5
	3100	8.3	7.2		2.3	
	3000	9.7	8.8		1.4	
170204a	7000	10.0	9.4	110	0.11	2.7
170204b	2800	9.6	8.1	270	2.1	3.5
170204c	6800	8.8	8.3	310	0.19	3.7
170204d <sup>e</sup>	2500	11.0	9.7	180	1.7	3.1
	3000	10.3	9.1		1.0	
170501	3400	9.2	8.2	240	1.0	3.4
170502a	3200	9.6	8.6	190	1.1	3.2
170502b <sup>d</sup>	13000	9.1	8.8	160	0.060	3.0

<sup>a</sup> Assuming meteoroids' impacts on the lunar surface at 20 km s<sup>-1</sup>

<sup>b</sup> The diameter of a disk with the same area as the cross-section of a radiating source

<sup>c</sup> The 1st-frame might be missed due to the frame drops. See text

<sup>d</sup> The exposure time and frame interval are 16.7 ms for 161107, 12.5 ms for 170502b, and 20.0 ms for the others

<sup>e</sup> Results for multiple successive frames are shown from top to bottom

We list the magnitudes in Table 4. It should be noted that there are ambiguities in these magnitudes because the brightness and spectrum of a flash would change significantly during the exposure of a video frame.

Luminous energy  $\mathcal{E}_{flash}$  observed at the top of the terrestrial atmosphere per unit area were calculated as

$$\mathcal{E}_{flash} = \sum [\int \bar{F}_{flash}(\lambda) R_{video}(\lambda) d\lambda] \cdot \Delta t, \quad (18)$$

where  $R_{video}(\lambda)$  is the response function of the typical video camera (Paper 1).  $R_{video}(\lambda)$  is non-zero between 310 and 1000 nm in wavelength, while the flash spectra would be reliable in 400–800 nm. Therefore, we used the best-fitted blackbody spectrum for  $\bar{F}_{flash}(\lambda)$  instead of the actual spectrum. The integrals were calculated numerically with  $d\lambda = 10$  nm.  $\Delta t$  is the exposure time for each frame, and the summation in Eq. (18) is calculated over the frames for which we obtained spectra.

The luminous energy of the source was obtained as

$$E_{flash} = \mathcal{E}_{flash} \cdot 4\pi r^2, \quad (19)$$

where  $r$  is the distance between the Moon and the observatory. We assume the flashes were radiated uniformly into  $4\pi$  steradians.

The impact energy, that is, the kinetic energy of the meteoroid, is obtained as

$$E_{imp} = E_{flash} / \eta, \quad (20)$$

where  $\eta$  is the luminous efficiency. Some studies (Belot Rubio et al. 2000a, b; Moser et al. 2010) show its

value between 0.1 and 0.2%. We adopted 0.2% in our calculations.

Though we examined the association between the flashes and meteoroid streams (Appendix), the origins of the impactors for the flashes are not clear. Therefore, we assume the typical impact velocity of 20 km s<sup>-1</sup> (McNamara et al. 2004) for simplicity in calculating the meteoroid masses for all the flashes. They are listed in Table 4.

A spectral flux density at some distance from a single blackbody of some specific temperature is proportional to the blackbody's cross-section perpendicular to the observers' line of sight. We assume that the blackbody spectra fitted to the observed spectra in Fig. 15 represent the spectral flux densities from radiating sources. The distance to the Moon is known. Then, we calculated the cross-sections. The cross-sections were converted to the diameters of disks with the same area (Table 4). The cross-sections are lower limits for the 1st-frames because a flash would be radiated from a larger area for a duration shorter than the exposure time. It should also be noted that the cross-sections could not represent the area of a single object, e.g., an incandescent crater floor, but the sum over many ejected hot particles.

We also calculated the crater diameters according to the formula for lunar craters up to roughly 100 m in diameter in loose soil or regolith developed by Gault (1974) and shown in Sect. 7.8 in a textbook (Melosh 1989). Impact energies are obtained from Eq. (20). The impact angles are assumed to be 45°; the most probable angle derived by Shoemaker

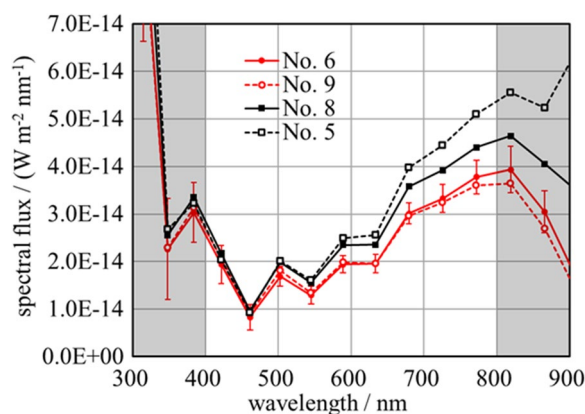


**Fig. 16** The effect of the incomplete spectral flat-field correction on a spectrum. We derived the spectra at the 2nd-frame of Flash 170201 with the four different reference points in a video frame for the spectral flat-field correction. The reference points are No. 6, 9, 8, and 5 in Fig. 14 in the increasing order of distance from the flash in a frame. The reference point for a comparison star was fixed to No. 5

(1962). We adopted the density of sporadic meteoroids,  $2.2 \times 10^3 \text{ kg m}^{-3}$  (Babadzhanov 2002), and lunar regolith,  $1.6 \times 10^3 \text{ kg m}^{-3}$  (McKay et al. 1991). These parameters result in crater diameters at the level of the preexisting lunar surface (apparent diameters) listed in Table 4.

#### Effect of incomplete spectral flat-field correction

As described in section "Spectral flat-field correction", the characteristics of spectral dispersion depend on the position of an image on a video frame. It was examined only for the nine points (reference points) over the frame (Fig. 14). For deriving spectra of Flash 170201, the comparison star was observed near the reference point No. 5. However, the flash image is not close to any reference points, though we used No. 6, which is closest to the flash image. Therefore, the correction could be incomplete and may result in inaccurate spectra.

To examine the effect of the incompleteness, we obtained the spectra using the other reference points for the flash, i.e., No. 9, 8, and 5, in increasing order of the distance. Figure 16 shows the result for the 2nd-frame of the flash. The temperatures of the blackbody spectra best fitted to these spectra are distributed between 3000 and 3200 K. We think that the incomplete correction would not seriously affect the spectra shown in Fig. 15 and the temperatures listed in Table 4.

#### Effect of atmospheric scintillation

Atmospheric scintillation, also called twinkling, is a temporal variation of an observed star brightness due to

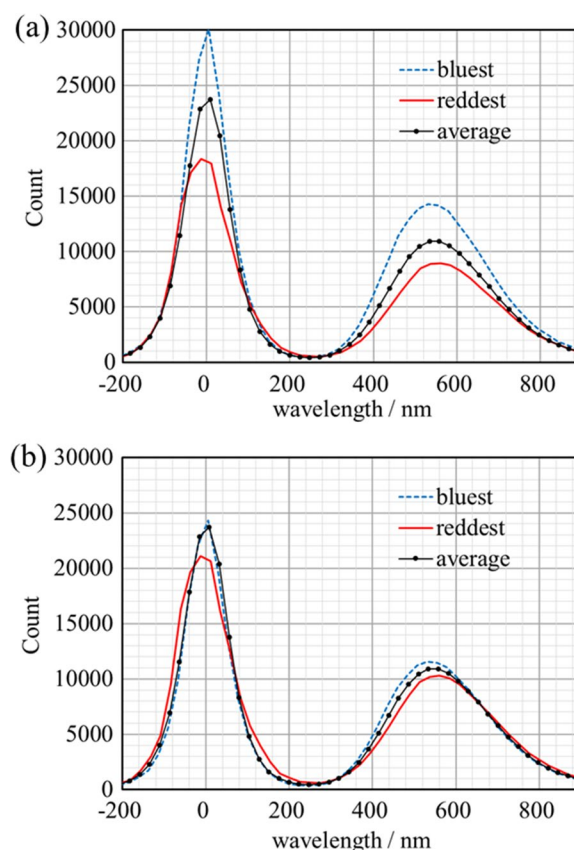


**Fig. 17** The effect of atmospheric scintillation on a spectrum of  $\beta$  Cet (Diphda). We recorded one hundred successive video frames with both the exposure time and frame interval of 20 ms and obtained count profiles along the zero-order and spectral images. **a** The broken blue line shows the profile for a frame when the star appears bluest in the one hundred frames. The solid red line shows the profile when the star appears reddest. The thin black line shows the average count profile over the one hundred frames. The plots along the average profile correspond to horizontal pixel positions in the averaged image (Fig. 10a). **b** The counts (y-axis values) were corrected as the total count is the same as that of the average profile to show the difference in the spectral waveform clearly

atmospheric turbulence. The frequency of the variation is typically of the order of 10 Hz. The scintillation would also cause the temporal variation of observed spectra. In ordinary astronomical observations, the effect of the variation is reduced due to long exposures. On the other hand, we obtain a flash spectrum for about 20 ms in exposure time for a video frame. Therefore, it is important to examine how much the effect is.

We observed a bright star,  $\beta$  Cet (Diphda), at  $54^\circ$  in zenith angle on Nov. 9, 2017, and recorded one hundred successive video frames. Both the exposure time of a frame and frame interval are 20 ms. An image averaged over the frames is shown in Fig. 10a. We obtained



the count profiles for each of the frames. Two of the profiles are shown in Fig. 17a with the profiles for the averaged image (Fig. 10a). Because the spectral dispersion direction by the grating is parallel to the local horizon, as depicted in Fig. 9b, we need not correct for the atmospheric dispersion. Therefore, the distance from the center of count of a zero-order image to a pixel along a spectral image is converted to a wavelength according to Eq. (1). Then, the count profiles are plotted as functions of wavelength.

In our observing system, the ratio of a zero-order count to the total count, including both the zero-order and spectral counts, increases with wavelength, as shown in Fig. 6b. Therefore, we can use the ratio to estimate the observed color of a star. Due to the atmospheric scintillation, the ratio changes from one frame to the next. We showed two profiles for which the ratio indicated bluest and reddest in the one hundred frames.

The total count (brightness) fluctuated with 13% in standard deviation around the mean count. To clearly show the spectrum's temporal variation, we divided each count in a profile by a constant (the profile's total count divided by the average profile's total count) (Fig. 17b). The effect of the scintillation seems to be significant at short wavelengths of 400–600 nm. However, it is less than 13% even in these two extreme profiles and 6% on average. Thus, the effect on color seems to be smaller than that on brightness.

Flashes 170201, 170204c, and 170204d were observed at 63° in zenith angle, larger than 54° at the  $\beta$  Cet observation. The variation could be larger in the observations of these flashes. The scintillation varies day by day, and the effect might be more significant in the flash observations than in the  $\beta$  Cet observation. Nevertheless, we expect that it would not make the spectra shown in Fig. 15 unreliable.

## Discussion

### Temporal variation of the spectra

The spectra of the three successive video frames of Flash 170201 (Fig. 15b) show the temporal decrease in temperature. Interestingly, the spectral flux integrated over wavelength is smaller in the 1st-frame than in the 2nd-frame. However, the smaller flux does not necessarily show the gradual increase in flux during the 1st- and 2nd-frames. As described in section "Comparison stars", the spectral flux is a temporal average over the exposure time. The flash would start near the end of the 1st-exposure with the sudden brightening. Therefore, the spectrum shows a high temperature, but the flux is low at the 1st-frame. We show the lightcurves of the three flashes that lasted more than a video frame in Additional file 3.

We also obtained successive spectra for Flash 170204d (Fig. 15f). The temperature increases by 500 K between the 1st- and 2nd-frames. However, we are unsure whether the difference is significant because of the low flux and considerable noise.

### Blue flashes

Three of the nine flashes in Fig. 15 are blue; that is, the spectral fluxes decrease almost monotonically with wavelength. This result contrasts with the 12 spectra observed on the 2018 Geminid lunar impact flashes (Paper I). None of them shows a clear blue spectrum. Temperatures derived from the multi-wavelength-band observations assuming blackbody spectra distribute over 1300–5800 K (Madedo et al. 2019a; Avdellidou and Vaubaillon 2019; Liakos et al. 2020) and are not as high as those of the three flashes. The blue flashes may not be the lunar flashes, but the reflections of the sunlight by bluish satellites or space debris. However, there is the following possibility of blue impact flashes.

The lunar impact flashes would be supposed to be red due to the following reasons. First, the thermal radiation from high-temperature liquid and solid ejecta generated at meteoroid's impact could dominantly contribute to the flashes. The evaporation temperatures of silicates are less than about 4000 K (Table II in Ahrens and O'Keefe (1972)). Therefore, the ejecta radiates at this or lower temperature. According to Wien's displacement law, the maximum in the blackbody spectrum of 4000 K occurs at a red wavelength of about 700 nm.

Second, the ejecta's red and infrared radiation was observed in laboratory impact experiments with particulate targets that simulate lunar regolith (Ernst and Schultz 2004, 2005). They shot Pyrex spheres of about 4 mm in diameter against pumice dust targets at about 5 km s<sup>-1</sup> and measured the light intensity of impact flashes at six wavelengths. They assumed blackbody radiation and derived the temperature. The temperature was about 3000–4000 K.

Third, a numerical simulation by Nemtchinov et al. (1998a, b) shows that the temperature of vapor cloud generated by the impact of a cm-size solid meteoroid on the solid lunar surface at 20 km s<sup>-1</sup> is less than 3000 K except at the beginning of the impact phenomena. In the beginning, the cloud is hotter. However, the radiation would occur underground due to the penetration of the meteoroid into the lunar regolith, and the radiation does not reach the lunar surface. Even after the cloud expands over the surface, the cool vapor envelope of lunar material may shroud the cloud (Artemieva et al. 2000). When the cloud disrupts the shroud and becomes observable, the expansion of the cloud reduces its temperature.

Fourth, the cloud may radiate at temperatures, e.g., more than 7000 K, for a short time. However, the duration is much shorter than the other processes that radiate, and the temporally integrated flux of this blue radiation would be negligible.

On the other hand, if a porous meteoroid hits a sizeable solid rock on the lunar surface, it does not penetrate deep. The amount of ejecta is smaller than the impacts of solid meteoroids against the regolith. Then, the contribution of the red radiation from the ejecta must be smaller. Hot dense cloud before the expansion radiates over the lunar surface. Therefore, we could observe it from the ground.

Artemieva et al. (2000) made a numerical simulation for a porous meteoroid of  $0.1 \text{ g cm}^{-3}$  in density in the case of Leonid's lunar impact. Their simulation models the lunar surface with solid granite. A vertical impact of a 1–10 cm size impactor at  $72 \text{ km s}^{-1}$  generates a hot vapor cloud expanding hemispherically over the lunar surface. The cool vapor envelope that shrouds the cloud does not appear. Thus, the hot cloud is observable.

Their simulation shows a short flash duration of about 0.1 ms (Artemieva et al. 2000), which is much shorter than the exposure time of our camera. At the same time, the blue flashes we observed appeared only in a frame (Table 2), indicating short durations. The absence of long-lasting blue flashes is concordant with the radiation from the hot gas cloud.

The density of the Geminid meteoroids is estimated to be highest in all meteoroid streams (Babadzhanov 2002). They would therefore penetrate deep into the regolith. The hot vapor cloud radiates underground and would not be observed. The low-temperature vapor of lunar material could shroud the cloud even after the cloud expands over the surface. Further, the amount of ejecta that radiates in red must be more significant than the case of low-density meteoroids. Thus, the high density of Geminids explains the absence of blue flashes in the period of Geminid activity.

On the other hand, the impacts of very porous meteoroids at velocities higher than, e.g.,  $50 \text{ km s}^{-1}$ , against sizable lunar rocks may have caused the three blue flashes. The diameters of spherical meteoroids calculated from the masses in Table 4 and an assumed density of  $2.2 \times 10^3 \text{ kg m}^{-3}$  are 5–10 cm. There would be many lunar rocks of these sizes or larger over the lunar regolith surface. Therefore, the chance of the small meteoroids hitting solid rocks may not be slight. However, the existence of blue flashes must be confirmed in the future by more than two observatories.

#### Future observations

Our spectral camera is simple. However, the analytical procedure to obtain spectra is complicated. The

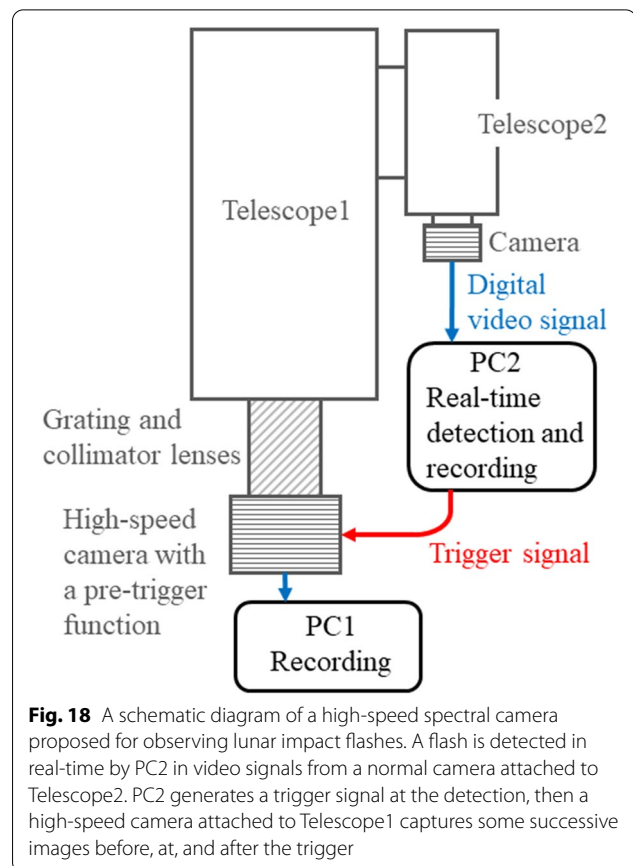


**Fig. 18** A schematic diagram of a high-speed spectral camera proposed for observing lunar impact flashes. A flash is detected in real-time by PC2 in video signals from a normal camera attached to Telescope2. PC2 generates a trigger signal at the detection, then a high-speed camera attached to Telescope1 captures some successive images before, at, and after the trigger

correction for the atmospheric dispersion described in section "[Corrections for the atmospheric dispersion](#)" is most cumbersome. The dispersion also makes the corrections for the 2nd-order image complicated. We need not make this correction if the spectral dispersion direction is parallel to the local horizon as shown in Fig. 9b and obtain the spectral image as shown in Fig. 10a. The mount of our telescope (Fig. 2) is an equatorial type, and the field of view rotates with time relative to the local horizon. Therefore, we recommend the use of an alt-azimuth mounting in future observations.

The grating used in our spectral camera is designed to diffract ultraviolet light most efficiently. Therefore, if we use a grating that is efficient at visible wavelengths, we can obtain brighter spectral images. It is also possible to make a spectral image longer and obtain higher spectral resolution keeping the brightness of the spectral image.

The time-scale of the early stage of lunar impact phenomena is  $5 \mu\text{s}$  if we calculate it as 100 mm in meteoroid size over  $20 \text{ km s}^{-1}$  in impact velocity. The time resolution of the present observation is not enough to study the stage in which the radiation from gases and plasma is essential. Even for the latter stage, where incandescent ejecta would radiate, the resolution is not enough.

Therefore, even a thousand-per-second framing rate helps to reveal the temporal variation of the flashes. We propose a high-speed spectral camera for future lunar flash observations (Fig. 18).

Telescope2 and a video camera monitor the night-side of the lunar disk. The video signal is transferred to a computer (PC2) for real-time detection of flashes. Once a flash is detected, some video frames before and after the flash are stored in its hard disk. An FPGA device may be used for the real-time detection of lunar flashes, as in a small Japanese space probe EQUULEUS (Fuse et al. 2019; Fujiwara et al. 2020; Funase et al. 2020), which is scheduled to be launched in 2022.

At the detection, a trigger signal generated by PC2 is sent to a high-speed camera. Most high-speed cameras recently have a pre-trigger function, enabling recording a pre-set number of frames before the trigger as well as frames after the trigger. After the recording in the camera, the frames are transferred to PC1 and stored in its hard disk. It is not practical to transfer and store frames continuously because the amount of data is huge.

A grating may be set just in front of the image sensor of the high-speed camera without collimator lenses as the spectral camera presented in this paper. To obtain high spectral resolutions, one may use an optical system consisting of a grating and lenses. A spectral image extends, then a zero-order image could be out of the field of view. The alignment of Telescopes 1 and 2 must be carefully calibrated in this case. Then, one would estimate the position of the zero-order image in a Telescope1 frame from the flash's position in a Telescope2 frame.

Due to the high framing rate, short exposure time decreases the camera's sensitivity for observing long-lasting phenomena, e.g., thermal radiation from ejecta that lasts more than 10 ms. However, obtaining time-resolved spectra for the early stage is important to study the mechanisms of the lunar impact flashes, even though we may lose spectra for the latter stages.

## Summary

We developed a simple spectral video camera to obtain the spectra of lunar impact flashes and detected ten flash candidates. Then, we derived the low-resolution spectra of nine of them with a temporal resolution of about 20 ms. In the derivation, corrections for the atmospheric dispersion were made because the spectral dispersion at the atmospheric refraction is not negligibly smaller than that by the grating. On the other hand, spectral images differ depending on where they appear in a video frame because of the non-uniformity of the grating. Therefore, we also made corrections for this position dependence as the “spectral flat-field correction”.

The time scale of the flashes is generally shorter than that of the atmospheric scintillation, which causes the twinkling of stars. We examined how the scintillation affects the spectral images observed by our camera. It was revealed that the scintillation would not significantly distort the waveforms of spectra in our observations.

Best-fitted single blackbody spectra show 2500–4200 K in temperature for six of the nine flashes. These temperatures are concordant with the results for the 2018 Geminid lunar impact flashes (Paper I) and the other results obtained by multi-wavelength-band observations. On the other hand, three of the nine flashes are blue; their spectral fluxes decrease almost monotonically with wavelength. It could be possible that an impact of a high-velocity porous meteoroid not against lunar soil but a solid rock generates blue radiation from high-temperature vapor.

The time resolution of our spectral camera is not high enough to study the temporal variations of the flashes. Therefore, we proposed a high-speed observing system with two telescopes. One telescope attached with a

**Table 5** Parameters of meteoroid streams

	N. Taurids	$\alpha$ -Centaurids	$\eta$ -Aquiriids	Sporadic
Radiant $\alpha^a$ [degree]	52	208	332	–
Radiant $\delta^a$ [degree]	21	–59	–3	–
ZHR <sub>(max)</sub> <sup>a</sup> or HR <sup>b</sup> for sporadic [meteors h <sup>–1</sup> ]	5	6	50	10
$\lambda_{\max}^a$ [degree]	230	319.2	45.5	–
$b^c$ [degree <sup>–1</sup> ]	0.026	0.18	0.08	–
$V^{a,d}$ [km s <sup>–1</sup> ]	29	56	66	17
$m_0^e$ [ $\times 10^{-6}$ kg]	1.0	0.062	0.031	9.8
$s^f$	1.90	1.75	1.95	2.19
$\gamma^g$	0.88	0.96	0.97	0.71
$\sigma$ or $\Xi^h$	1	1	1	–

Besides these parameters, we set the detection limit to be  $4 \times 10^4$  J for the luminous energy of lunar impact flash sources and the conversion efficiency from meteoroid kinetic energy to luminous energy to be 0.2%

<sup>a</sup> IMO Meteor Shower Calendar (2021)

<sup>b</sup> Liakos et al. (2020)

<sup>c</sup> The slope of ascending and descending activity profiles: Table 3b in Jenniskens (1994)

<sup>d</sup> Geocentric velocity

<sup>e</sup> Meteoroid mass that corresponds to a terrestrial meteor of 6.5 in magnitude calculated from Eqs. (1) and (2) in Hughes (1987)

<sup>f</sup> Mass index of the shower, which is connected to the population index  $r$  as  $s = 1 + 2.5 \log_{10} r$

<sup>g</sup> The quotient between the gravitational focusing factors of the Earth and the Moon

<sup>h</sup> The distance between the Earth and the stream center divided by the distance between the Moon and the center

**Table 6** Association with meteoroid streams

Flash	Solar longitude $\lambda^a$	Considered stream	Impact angle <sup>b</sup>	Probability in %
161107	225	N. Taurids	60	68
170201	313	$\alpha$ -Centaurids	17	13
170204a	316	$\alpha$ -Centaurids	25	43
170204b	316	$\alpha$ -Centaurids	19	38
170204c	316	$\alpha$ -Centaurids	48	58
170204d	316	$\alpha$ -Centaurids	−11	–
170501	41	$\eta$ -Aquariids	−21	–
170502a	42	$\eta$ -Aquariids	21	43
170502b	42	$\eta$ -Aquariids	17	38
170502c	42	$\eta$ -Aquariids	23	45

<sup>a</sup> The solar longitudes at the time of detections in degree<sup>b</sup> The angle measured from local horizons in degree

normal video camera detects flashes. A computer makes the detection in real-time; then, it generates a trigger signal for a high-speed spectral camera attached to the other larger telescope. A high framing rate would show the spectral evolution of impact flashes and the associated temperature signal more clearly than is possible with the video system presented in this work.

### Appendix: Origin of the impactors

Assuming that the flashes in Table 2 are lunar phenomena, we calculated their probability of being associated with some meteor streams according to the formulae proposed by Madiedo et al. (2015, 2019b). For simplicity, we assumed only one most probable stream for a flash and the sporadic background and did not consider other streams that might be the flash sources. The probability of a lunar impact flash associated with that stream is then expressed as

$$p^{ST} = \frac{N^{ST}}{N^{ST} + N^{SPO}}, \quad (21)$$

where  $N^{ST}$  is the number of impacts that the stream can produce.  $N^{SPO}$  is the number of impacts that the sporadic background can produce. We calculate the former based on the maximum ZHR (Zenithal Hourly Rate) of the stream observed on the Earth. The latter is calculated mainly from the HR (hourly rate) of sporadic meteors. Because the formulae to obtain these values are complicated, we just show our parameters for Eq. (14) in Madiedo et al. (2015) or Eq. (6.28) in Madiedo et al. (2019b) in Tables 5 and 6.

We considered Northern Taurids for Flash 161107,  $\alpha$ -Centaurids for the flashes detected in early February, and  $\eta$ -Aquariids for the flashes detected in early May. In the case of the impacts of these streams, we show the impact angles measured from local lunar horizons in Table 6. Negative values mean that the flashes occurred in the area where no stream-associated meteoroids could impact the lunar surface; that is, the stream cannot be the source of the flash. Table 6 shows the probabilities of the flashes being associated with the streams.

### Supplementary Information

The online version contains supplementary material available at <https://doi.org/10.1186/s40623-022-01575-9>.

**Additional file 1: Additional\_video\_file.** Flash candidate 170201. We converted successive ten frames in a raw SER format video file to FITS format images. Then, we increased the brightness and contrast of these images with fixed parameters. Next, we made an animated GIF file of 5 frames  $s^{-1}$  in framing rate with these images. Finally, we pasted the animation on the PowerPoint slide.

**Additional file 2: Additional\_figure\_file1.** Spectra of the stars obtained by comparing their observed count profiles as functions of wavelength with that of  $\alpha$  And. See the text in the file for details.

**Additional file 3: Additional\_figure\_file2.** Lightcurves of the three flashes that lasted more than a video frame. See the text in the file for details.

**Additional file 4.** Additional\_SER\_video\_files: The spectra of Flash 170201 can be derived from these files. We cropped the video frames to reduce the file sizes. Ser-format videos can be viewed by an open-source application, “SER Player (2021)” (1) Flash170201.ser: Flash 170201. The flash appears in the 51st-frame. The bright area at the upper right is the Aristarchus area. The original frame size is  $960 \times 592$  pixels. We extracted one hundred frames of  $200 \times 200$  pixels in size. The coordinate of their upper-left pixel is (670, 290) in the original frames, in which the coordinate of the upper-left pixel is (0, 0). We averaged 495 frames while shifting images to compensate for slight image motion in obtaining the background image. Therefore, the analyses of this cropped video may lead to slightly different results from ours. (2) TYC4665-715-1.ser: Comparison star. A faint star at the lower left is TYC4665-463-1. The original frame size is  $960 \times 592$  pixels. We extracted one hundred frames of  $120 \times 100$  pixels in size. The coordinate of their upper-left pixel is (355, 315) in the original frames. We averaged all frames while shifting images to compensate for slight image motion. (3) alpha-And\_No5.ser:  $\alpha$  And recorded at the center of the original video frames. The original frame size is  $1936 \times 1216$  pixels. We extracted one hundred frames of  $120 \times 100$  pixels in size. The coordinate of their upper-left pixel is (870, 538) in the original frames. We discarded five bad frames and averaged the other frames while shifting images to compensate for slight image motion. (4) alpha-And\_No6.ser:  $\alpha$  And recorded near the right edge of the original video frames. The original frame size is  $1936 \times 1216$  pixels. We extracted one hundred frames of  $120 \times 100$  pixels in size. The coordinate of their upper-left pixel is (1780, 538) in the original frames. We discarded one bad frame and averaged the other frames while shifting images to compensate for slight image motion. (5) dark\_for\_Flash170201.ser, dark\_for\_TYC4665-715-1.ser, dark\_for\_alpha-And\_No5.ser, dark\_for\_alpha-And\_No6.ser: Dark frames for the SER videos mentioned above. These were recorded while we covered the camera with an opaque cap. The camera settings were the same between the non-dark and dark videos.

**Additional file 5.** Additional\_tool\_files1: Source files of “ser\_reduction.” This tool was used to subtract the dark frames from the SER format videos. Two header files (.h), four source files (.cpp), and a resource file (.rc) were



built to create the executable file `ser_reduction.exe` by Visual Studio 2017 for  $\times 86(32\text{bit})$  Windows personal computers (The same applies hereafter). The comments in the source files are written in Japanese (The same applies hereafter).

**Additional file 6.** `Additional_tool_files2`: Source files of "`ser_to_fits_csv`." This tool was used to extract a part of a frame where a lunar impact flash was recorded in an SER format video. The extracted image is saved as a CSV format file that can be loaded in Excel. It can also be saved as a FITS format file. Two header files (.h), five source files (.cpp), and a resource file (.rc) were built to create the executable file `ser_to_fits_csv.exe`.

**Additional file 7.** `Additional_tool_files3`: Source files of "`ser_average_adjust`." This tool was used to average frames in an SER format video to obtain a lunar background image, which was subtracted from an image of a flash. This tool allows us to average frames while shifting images to best match with a reference frame. Two header files (.h), six source files (.cpp), and a resource file (.rc) were built to create the executable file `ser_average_adjust.exe`.

**Additional file 8.** `Additional_tool_files4`: Source files of "`ser_average_select`." This tool was used to average frames in an SER format video to obtain an averaged stellar image. This tool allows us to select frames of good quality manually. In addition, this tool allows us to shift images in the averaging process. Two header files (.h), six source files (.cpp), and a resource file (.rc) were built to create the executable file `ser_average_select.exe`.

**Additional file 9.** The spectra of Flash170201 were calculated using these EXCEL files. (1) `Flash170201.xlsx`: An EXCEL file used to obtain the spectra. (2) `TYC4665-715-1.xlsx`: An EXCEL file used to obtain the count profile of the comparison star, TYC4665-715-1. We pasted the count profile to a sheet in `Flash170201.xlsx`. (3) `alpha-And_No5.xlsx`, `alpha-And_No6.xlsx`: Two EXCEL files to obtain the count profiles of  $\alpha$  And at different positions in the video frames. We used the count profiles in the spectral flat-field correction (see section "`Spectral flat-field correction`"). We pasted the count profiles to a sheet in `Flash170201.xlsx`.

## Acknowledgements

We are indebted to the students of the Univ. Electro-Comm. for their efforts in the observations. We also thank two anonymous reviewers for their very useful comments.

## Authors' contributions

MY designed the spectral camera and supervised the observations by the graduate and undergraduate students of the Univ. Electro-Comm. He also developed methodologies and applications for analyzing the data. He analyzed the data, conducted the investigation, and wrote the original draft. FK made the spectral camera and made observations. He also developed applications for detecting the lunar impact flashes in the video data. He analyzed the data and conducted the investigation. Both authors read and approved the final manuscript.

## Authors' information

MY retired from the Univ. Electro-Comm. in 2019 and is a professor emeritus of the university. He received a Ph.D. for his study in geophysics from the Univ. Tokyo in 1983. He is a member of the Japanese Society of Planetary Sciences, AGU, and IAU. He published some papers on lunar impact flashes and laboratory impact experiments. FK was a graduate student supervised by MY in the university during the research activities.

## Funding

The authors declare that there is no source of funding for the research reported.

## Availability of data and materials

We present the raw SER format video data and EXCEL files used in our analyses for Flash 170201 as Additional files. In addition, the software tools for processing video data with their source files are also included as Additional files. The amount of data for all the flashes is huge. Besides, this paper aims to present

the detail of the camera and the analytical procedures of the videos. Therefore, we do not present the raw data for the other flashes.

## Declarations

### Ethics approval and consent to participate

Not applicable.

### Consent for publication

Not applicable.

### Competing interests

The authors declare that they have no known competing financial interests or personal relationships that could have appeared to influence the work reported in this paper.

### Author details

<sup>1</sup>Department of Engineering Science, The University of Electro-Communications, 1-5-1 Chofugaoka, Chofu-shi, Tokyo 182-8585, Japan. <sup>2</sup>Present Address: Tama-shi, Tokyo 206-0034, Japan.

Received: 5 August 2021 Accepted: 8 January 2022

Published online: 25 April 2022

## References

- Ahrens TJ, O'Keefe JD (1972) Shock melting and vaporization of lunar rocks and minerals. *Moon* 4:214–249. <https://doi.org/10.1007/BF00562927>
- Artemieva NA, Shuvalov VV, Trubetskaya IA (2000) Lunar Leonid meteors—Numerical simulations. 31st Lunar and Planetary Science Conference, Abstract No. 1402
- Avdellidou C, Vaubaillon J (2019) Temperatures of lunar impact flashes: mass and size distribution of small impactors hitting the Moon. *Mon Not R Astron Soc* 484:5212–5222. <https://doi.org/10.1093/mnras/stz355>
- Babadzhanov PB (2002) Fragmentation and densities of meteoroids. *Astron Astrophys* 384:317–321. <https://doi.org/10.1051/0004-6361/20020010>
- Bellot Rubio LR, Ortiz JL, Sada PV (2000a) Luminous efficiency in hypervelocity impacts from the 1999 Lunar Leonids. *Astrophysical J* 542:L65–L68. <https://doi.org/10.1086/312914>
- Bellot Rubio LR, Ortiz JL, Sada PV (2000b) Observation and interpretation of meteoroid impact flashes on the Moon. *Earth Moon Planets* 82–83:575–598. <https://doi.org/10.1023/A:1017097724416> (1998 for the online version)
- Bessell MS (2005) Standard photometric systems. *Annu Rev Astron Astrophys* 43:293–336. <https://doi.org/10.1146/annurev.astro.41.082801.100251>
- Bonanos AZ, Avdellidou C, Liakos A, Xilouris EM, Dapergolas A, Koschny D, Bellas-Velidis I, Boumis P, Charmandaris V, Fytisil A, Maroussis A (2018) NELIOTA: first temperature measurement of lunar impact flashes. *Astron Astrophys* 612(A76):6. <https://doi.org/10.1051/0004-6361/201732109>
- Dunham DW, Cudnik B, Palmer DM, Sada PV, Melosh J, Beech M, Frankenberg R, Pellerin L, Venable R, Asher D, Sterner R, Gotwols B, Wun B, Stockbauer D (2000) The first confirmed videorecordings of lunar meteor impacts. 31st Lunar and Planetary Science Conference, Abstract No. 1547
- Ernst CM, Schultz PH (2004) Early-time temperature evolution of the impact flash and beyond. 35th Lunar and Planetary Science Conference, Abstract No. 1721
- Ernst CM, Schultz PH (2005) Investigations of the luminous energy and luminous efficiency of experimental impacts into particulate targets. 36th Lunar and Planetary Science Conference, Abstract No. 1475
- Flower PJ (1996) Transformations from theoretical Hertzsprung-Russell diagrams to color-magnitude diagrams: effective temperatures, B-V colors, and bolometric corrections. *Astrophys J* 469:355–365. <https://doi.org/10.1086/177785>
- Fujiwara M, Ikari S, Kondo H, Fuse R, Masuda Y, Abe S, Yanagisawa M, Yamamoto K, Yano H, Funase R (2020) Development of on-board image processing algorithm to detect lunar impact flashes for DELPHINUS. *Trans Japan Soc Aero Space Sci* 63(6):265–271. <https://doi.org/10.2322/tjsass.63.265>
- Funase R et al (2020) Mission to Earth-Moon Lagrange Point by a 6U CubeSat: EQUULEUS. *IEEE Aerosp Electron Syst Mag* 35:30–44. <https://doi.org/10.1109/MAES.2019.2955577>

- Fuse R, Abe S, Yanagisawa M, Funase R, Yano H (2019) Space-based observation of lunar impact flashes. *Trans Japan Soc Aero Space Sci Aerosp Technol Jpn*. 17(3):315–320. <https://doi.org/10.2322/tastj.17.315>
- Gault DE (1974) Impact cratering. In: Greeley R, Schultz PH (ed) *A Primer in lunar geology*. NASA Ames: 137–175
- Hughes DW (1987) P/Halley dust characteristics: a comparison between Orionid and Eta Aquarid meteor observations and those from the flyby spacecraft. *Astron Astrophys* 187:879–888
- Jenniskens P (1994) Meteor stream activity I. The annual streams. *Astron Astrophys* 287:990–1013
- Kurosawa K, Kadono T, Sugita S, Shigemori K, Sakaiya T, Hironaka Y, Ozaki N, Shiroshita A, Cho Y, Tachibana S, Vinci T, Ohno S, Kodama R, Matsui T (2012) Shock-induced silicate vaporization: the role of electrons. *J Geophys Res* 117(E4):14. <https://doi.org/10.1029/2011JE004031>
- Liakos A, Bonanos AZ, Xilouris EM, Koschny D, Bellas-Velidis I, Boumis P, Charmandaris V, Dapergolas A, Fytisilis A, Maroussis A, Moissl R (2020) NELIOTA: methods, statistics, and results for meteoroids impacting the Moon. *Astron Astrophys* 633(A112):29. <https://doi.org/10.1051/0004-6361/201936709>
- McNamara H, Suggs R, Kauffman B, Jones J, Cooke W, Smith S (2004) Meteoroid engineering model (MEM): a meteoroid model for the inner solar system. *Earth Moon Planets* 95:123–139. Doi: 10.1007/s11038-004-9044-8.
- Madiedo JM, Ortiz JL, Organero F, Ana-Hernández L, Fonseca F, Morales N, Cabrera-Caño J (2015) Analysis of Moon impact flashes detected during the 2012 and 2013 Perseids. *Astron Astrophys* 577(A118):9. <https://doi.org/10.1051/0004-6361/201525656>
- Madiedo JM, Ortiz JL, Morales N, Santos-Sanz P (2019a) Multiwavelength observations of a bright impact flash during the 2019 January total lunar eclipse. *Mon Not R Astron Soc* 486:3380–3387. <https://doi.org/10.1093/mnras/stz932>
- Madiedo JM, Ortiz JL, Yanagisawa M, Aceituno J, Aceituno F (2019b) Impact flashes of meteoroids on the Moon. In: Ryabova GO, Asher DJ, Campbell-Brown MD (ed) *Meteoroids*. Cambridge Univ. Press: 136–158. <https://doi.org/10.1017/9781108606462>
- McKay DS, Heiken G, Basu A, Blanford G, Simon S, Reedy R, French BM, Papike J (1991) The lunar regolith. In: Heiken GH, Vaniman DT, French BM (ed) *Lunar sourcebook*. Cambridge Univ. Press: 285–356.
- Melosh HJ (1989) *Impact cratering: a geologic process*. Oxford Univ Press, New York, pp. 245. <https://doi.org/10.1017/S0016756800007068>
- Montanes-Rodriguez P, Palle E, Goode PR (2007) Measurements of the surface brightness of the earthshine with applications to calibrate lunar flashes. *Astron J* 134:1145–1149. <https://doi.org/10.1086/519736>
- Moser DE, Suggs RM, Swift WR, Suggs RJ, Cooke WJ, Diekmann AM, Koehler HM (2010) Luminous efficiency of hypervelocity meteoroid impacts on the Moon derived from the 2006 Geminids, 2007 Lyrids, and 2008 Taurids. In: *Proceedings of the Meteoroids 2010 Conference*, NASA CP-2011-216469: 142–154
- Nemtchinov IV, Shuvalov VV, Artemieva NA, Ivanov BA, Kosarev IB, Trubetskaya IA (1998a) Light flashes caused by meteoroid impacts on the lunar surface. *Sol Syst Res* 32:99–114
- Nemtchinov IV, Shuvalov VV, Artemieva NA, Ivanov BA, Kosarev IB, Trubetskaya IA (1998b) Light impulse created by meteoroids impacting the Moon. 29th Lunar and Planetary Science Conference, Abstract No. 1032
- Ortiz JL, Aceituno FJ, Aceituno J (1999) A search for meteoritic flashes on the Moon. *Astron Astrophys* 343:L57–L60
- Ortiz JL, Sada PV, Bellot Rubio LR, Aceituno FJ, Aceituno J, Gutierrez PJ, Thiele U (2000) Optical detection of meteoroidal impacts on the Moon. *Nature* 405:921–923. <https://doi.org/10.1038/35016015>
- Schubert G, Walterscheid RL (1999) Earth. In: Cox AN (ed) *Allen's astrophysical quantities*, 4th edn. Springer, New York, pp 239–292
- Schultz PH, Eberhardy CA (2015) Spectral probing of impact-generated vapor in laboratory experiments. *Icarus* 248:448–462. <https://doi.org/10.1016/j.icarus.2014.10.041>
- Suggs RM, Moser DE, Cooke WJ, Suggs RJ (2014) The flux of kilogram-sized meteoroids from lunar impact monitoring. *Icarus* 238:23–36. <https://doi.org/10.1016/j.icarus.2014.04.032>
- Shoemaker EM (1962) Interpretation of lunar craters. In: Kopal Z (ed) *Physics and astronomy of the Moon*. Academic Press, New York: 283–359. <https://doi.org/10.1016/C2013-0-12487-7>
- Xilouris EM, Bonanos AZ, Bellas-Velidis I, Boumis P, Dapergolas A, Maroussis A, Liakos A, Alikakos I, Charmandaris V, Dimou G, Fytisilis A, Kelley M, Koschny D, Navarro V, Tsiganos K (2018) NELIOTA: the wide-field, high-cadence, lunar monitoring system at the prime focus of the Kryoneri telescope. *Astron Astrophys* 619(A141):14. <https://doi.org/10.1051/0004-6361/201833499>
- Yanagisawa M, Kakinuma F (2022) Ser\_scan: A software tool for detecting lunar impact flashes in SER format videos. *Bulletin of the University of Electro-Communications* 34: pp. 6. in press. [https://uec.repo.nii.ac.jp/?action=repository\\_opensearch&index\\_id=7](https://uec.repo.nii.ac.jp/?action=repository_opensearch&index_id=7)
- Yanagisawa M, Kisaichi N (2002) Lightcurves of 1999 Leonid impact flashes on the Moon. *Icarus* 159:31–38. <https://doi.org/10.1006/icar.2002.6931>
- Yanagisawa M, Ohnishi K, Takamura Y, Masuda H, Sakai Y, Ida M, Adachi M, Ishida M (2006) The first confirmed Perseid lunar impact flash. *Icarus* 182:489–495. <https://doi.org/10.1016/j.icarus.2006.01.004>
- Yanagisawa M, Ikegami H, Ishida M, Karasaki H, Takahashi J, Kinoshita K, Ohnishi K (2008) Lunar impact flashes by Geminid meteoroids in 2007. 71st Annual Meteoritical Society Meeting, Meteoritics and Planetary Sciences 43, Nr 7, Supplement A174: Abstract 5169
- Yanagisawa M, Uchida Y, Kurihara S, Abe S, Fuse R, Tanaka S, Onodera K, Yoshida F, Chi H, Lin Z, Lee J, Kawamura T, Yamada R (2021) Low dispersion spectra of lunar impact flashes in 2018 Geminids. *Planet Space Sci* 195:12. <https://doi.org/10.1016/j.pss.2020.105131>

#### Online database

- FireCapture. <http://www.firecapture.de/>. Accessed 10 Nov 2021
- IMO Meteor Shower Calendar. <https://www.imo.net/resources/calendar/>. Accessed 10 Nov 2021
- MODTRAN. <http://modtran.spectral.com/>. Accessed 10 Nov 2021
- SER Player. <https://sites.google.com/site/astropipp/ser-player>. Accessed 10 Nov 2021
- SIMBAD. <https://simbad.u-strasbg.fr/simbad/>. Accessed 10 Nov 2021
- Space-Track. <https://www.space-track.org/>. Accessed 10 Nov 2021
- StellaNavigator. <https://www.astroarts.co.jp/products/software.shtml>. Accessed 10 Nov 2021
- Virtual Moon Atlas. <https://www.ap-i.net/avl/en/start/>. Accessed 10 Nov 2021

#### Publisher's Note

Springer Nature remains neutral with regard to jurisdictional claims in published maps and institutional affiliations.

**Submit your manuscript to a SpringerOpen<sup>®</sup> journal and benefit from:**

- Convenient online submission
- Rigorous peer review
- Open access: articles freely available online
- High visibility within the field
- Retaining the copyright to your article

Submit your next manuscript at ► [springeropen.com](https://www.springeropen.com)